A set of canonical problems in sloshing. Part 2: Influence of tank width on impact pressure statistics in regular forced angular motion

A. Souto-Iglesias [a,*], G. Bulian [b], E. Botia-Vera [c]

[a] CEHINAV Res.Gr., DMFPA, ETSIN, Technical University of Madrid (UPM), 28040 Madrid, Spain
[b] Department of Engineering and Architecture, University of Trieste, Via A. Valerio 10, 34127, Trieste, Italy
[c] CEHINAV Res.Gr., ETSIN, UPM, 28040 Madrid, Spain

ARTICLE INFO

Accepted 10 June 2015

Keywords:
Sloshing experiments
Impact pressure
Statistics
Two-dimensionality

ABSTRACT

Continuing along the path of previous papers in this series, the present paper addresses, experimentally, sloshing in a rectangular tank under harmonic angular forcing. Since lateral and roof impacts are relevant in sloshing assessment and present distinct dynamics, these have been studied. Water and oil have been used in order to obtain data for high and moderate Reynolds numbers. With the aim of addressing effects induced by the three-dimensionality of the flow, a study of the influence of the tank width on pressure statistics has also been conducted. For this purpose, a tank which can be adjusted to 4 different widths by replacing the side plates was built. For each combination of fluid, tank width and filling level, a total of 120 experiments, each comprising 120 peaks, have been conducted, allowing an analysis in time and ensemble domains to be performed. Impact pressure statistics are presented including mean values, percentiles, and exceedance probability graphs.

1. Introduction

State-of-the-art sloshing assessment procedures for LNG vessels and floating production and storage units are based on risk assessment techniques (DNV, 2006; LRS, 2009; de Sgraveeze and Maillard, 2009; Kuo et al., 2009; Diebold, 2010). In such procedures, the statistical characterization of the sloshing loads relies on data obtained from experimental campaigns. Significant material and human resources need to be allocated in order to carry out these campaigns. Nonetheless, obtaining comparable results from different facilities is still an open problem (Kim et al., 2012; Loysel and Chollet, 2012; Loysel, 2013). Due to the extra costs that derive from these campaigns, a mid-term goal of designers is to characterize sloshing loads using CFD technologies.

A widely known attempt to assess the capabilities of CFD codes to achieve this target emerged from the Special 1st "Sloshing Dynamics" Symposium at ISOPE-2009 Conference, in which a benchmark test case was proposed to all participants (Kim et al., 2009). Contributions were presented using commercial codes (Godderidge et al., 2009) and meshless methods (Rafiee et al., 2009). Although this initiative was ground breaking, the outcomes have been limited because, for the chosen configurations, the phenomena are still, to this day, too complex to be modeled with state-of-the-art CFD technologies. In order for the experimental results to represent a usable and reliable benchmark for CFD tools validation, the approach undertaken herein is, on the one hand, to simplify the experimental setup and, on the other hand, to seek for the highest possible experimental repeatability. With this in mind, the simple geometry of a rectangular tank subjected to harmonic roll motion was chosen as the testing configuration. Details of the rig setup as well as data acquisition systems and procedures were presented in the part 0 paper of the series (Souto-Iglesias et al., 2011) while simulation of lateral impacts with Smoothed Particle Hydrodynamics (SPH), for this same rectangular, tank were conducted in the part 1 paper (Delorme et al., 2009).

Sloshing experiments using regular excitations may be of limited use due to the high nonlinearity of the sloshing phenomena. Notwithstanding this, transfer functions for narrow banded sea spectra have been elaborated by authors such as Gran (1981), and a regular excitation analysis is used in the pre-screening phases of LNG sloshing assessment procedures by important stake-holders such as Hyundai, which is the leading LNG carriers shipbuilder (Park et al., 2011). Harmonic motions were also used by Kim et al. (2010), who performed both 2D regular motion and 3D irregular motion experiments. They statistically analyzed different properties of impacts (impact pressure, rising time, duration, etc.) through scatter plots and distribution fitting. However, the type of experimental data presented therein did not allow a direct comparison

* Corresponding author.
E-mail address: antonio.souto@upm.es (A. Souto-Iglesias).

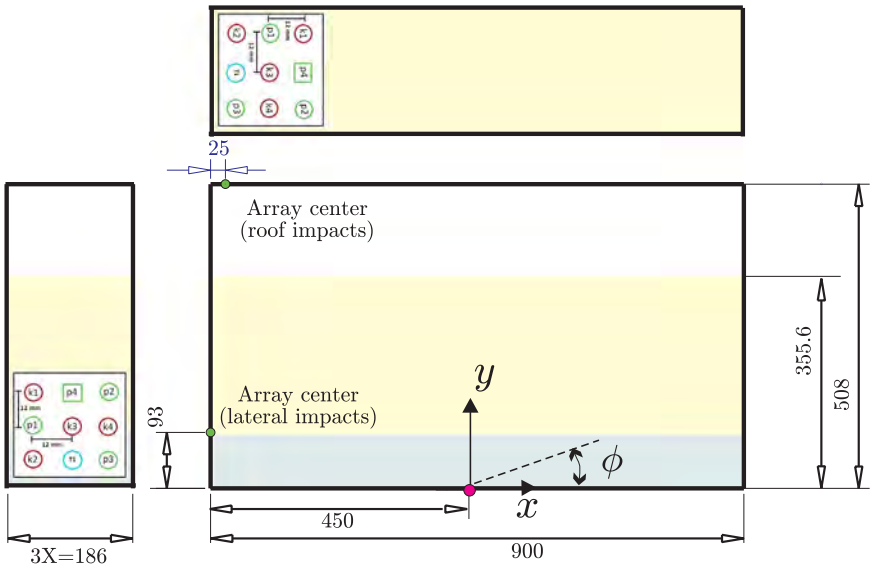

Fig. 1. Schematic of tank dimensions (mm), liquid levels, and sensor array positions for lateral and roof impacts. Sensor array not to scale with the rest of the figure. Filling level precision is ± 1 mm.

between the two-dimensional and the three-dimensional case, due to the differences in tanks and forcing.

Chen et al. (2013) recently published experimental data obtained with regular angular motion sloshing tests, focusing on run-up events, and used this data to validate their own SPH method simulations. More interestingly, regular motion impacts can be used to systematically explore the low probability levels of certain types of impacts, such as those arising from the influential SLOSHEL JIP project elementary loading processes (ELPs) taxonomy (Lafeber et al., 2012).

Furthermore, Song et al. (2013) recently investigated the kinematics and dynamics of sloshing impact events using regular motions, looking at the correlation between impact pressures and velocities, with the latter measured by means of the bubble image velocimetry (BIV) technique. Focussing on a single specific excitation case, they were able to find consistent pressure–velocity correlations and substantially different correlation factors depending on whether lateral or roof impacts were considered.

In regard to sloshing physics in general, significant contributions are due to Lugni et al. (2006, 2010a), who described the extraordinary accelerations associated to wave impact events. Their work is nonetheless not specifically devised so as to be useful as a reference for CFD validation attempts.

If the focus is put on to the statistical characterization of sloshing pressures, major contributions are due to Graczyk and Moan (2008) and Graczyk et al. (2007) who provided a statistical fitting for long series of sloshing impact pressure recordings aimed at building simplified models of sloshing events load histories for structural finite element analysis.

Repeatability in sloshing tests has not received much attention in the literature. Bogaert et al. (2010) paid attention to wave heights during single impact experiments within the SLOSHEL project, finding variation coefficients of the order of 1%. Kimmoun and Brosset (2010), in the framework of the same project, looked at pressure records but with a limited set of repetitions, not large enough to obtain general conclusions. More recently, the authors of the present paper have investigated the transient and stationary characteristics of impact pressure under regular angular motion (Bulian et al., 2014). They found that, for the analyzed case, individual peaks could be considered independent identically distributed (i.i.d.) random variables. This implies that the statistics obtained during a single experiment were comparable to those

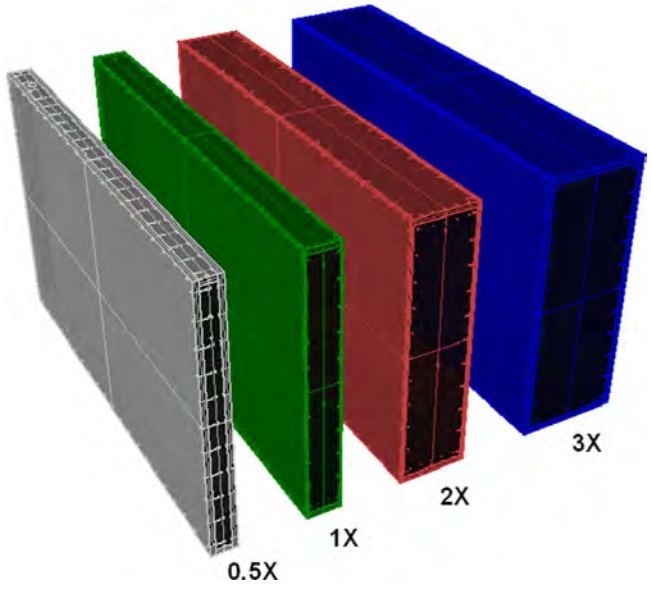

Fig. 2. Schematics of tanks with different analyzed widths.

obtained for individual peaks along successive repetitions. This practical ergodicity is taken for granted in the industry when data from different experiments is packed together and extremely long run data sets are obtained (e.g. Fillon et al., 2013). Bulian et al. (2014) also found a strong influence of relatively minor variations of the excitation frequency on the statistics, which is consistent with the strongly nonlinear behavior of shallow water sloshing flows analyzed by e.g. Bouscasse et al. (2013). On the other hand, the influence of the sensor type on statistics, though not discussed in depth, was found not to be substantial, at least in qualitative terms.

With the aim of addressing the influence that experimental uncertainties may have on extreme pressure peaks statistics, sensitivity of impact pressures statistics to minor variations in the experimental setup and parameters (filling levels, motion amplitudes, etc.) is recently receiving more attention. As examples of such efforts, and within the framework of a benchmark led by GTT (Loysel and Chollet, 2012; Loysel, 2013), Mehl and colleagues looked at the influence of motion characteristics (Mehl et al., 2013)

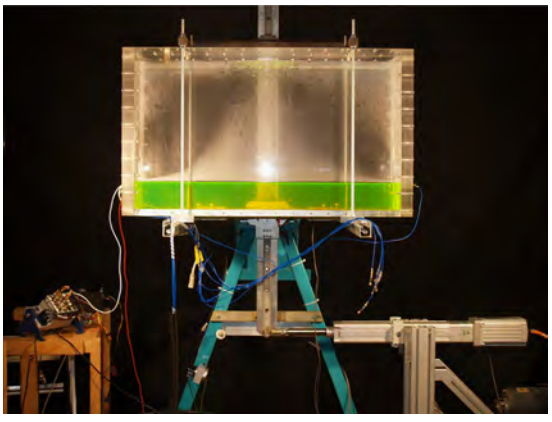

Fig. 3. Rig and actuator setup.

Fig. 4. Dynamic piezo-electric (PCB 112A21) (top) (Piezotronics, 2008) and piezo-resistive pressures sensors (Kulite-Xtel-190(M)) (bottom) (Kulite, 2014).

Table 1
Physical properties of the liquids: ρ for density, μ for the dynamic viscosity, ν for the kinematic viscosity, σ for surface tension, c_s for sound speed.

Liquid	ρ (kg/m^3)	μ (kg/m/s)	ν (m^2/s)	σ (kg/s^2)	c_s (m/s)
Water	998	8.94e−4	8.96e−7	0.0728	1480
Oil	900	0.045	5e−5	0.033	1450

and filling levels (Mehl et al., 2014) on such statistics. Within the conditions considered in the benchmark, the single impact ones were selected for the motion sensitivity analysis. The influence of motion amplitude, period, and basic motion formula were analyzed. The shape of the free surface during the events and the impact pressure average values were shown to significantly depend on such minor variations. Regarding the filling level sensitivity, Mehl et al. (2014) found, once again for single impact conditions, that filling level variations of the order of 1 mm at model scale did not produce any significant effects on impact pressure statistics. A similar analysis was carried out by Neugebauer et al. (2014) who, in turn, found a significant influence for filling level differences of around $\pm$ 1 mm (on fillings of the order of 800 mm). However, their quantitative analysis of the sensitivity of the results to the filling level may have been too limited in order to consider their outcomes clear and conclusive.

Interesting sensitivity analyses have also been conducted by Choi et al. (2010, 2012) and by Pistani and Thiagarajan (2012). They looked at the influence of minor variations in the mounting (flushness) of the sensors. According to Choi et al. (2010, 2012), mounting differences as small as 1 mm could induce a large influence on the pressure registers; Pistani and Thiagarajan did not, on the other hand, find such a strong dependence.

Regarding the two-dimensionality of the flow in planar motion sloshing impacts, Schreier and Mehl (2012) provided some insight into the matter. They used translational motions with two tanks of different widths within the aforementioned ISOPE 2012 benchmark (Loysel and Chollet, 2012) finding larger pressures with the thinner tank. This aspect is relevant since the CFD codes used for these problems are, for the moment, usually run considering 2D flows, with their outcomes validated through a comparison with real experiments in which the actual two-dimensionality of the flow is not discussed in depth. Along the same line, but comparing, using regular motions, a 3D model of a membrane tank and a section of such tank, Kim et al. (2013) looked at the influence of such full 3D and 2D configurations on the top 10% impact pressure average values. They found the 3D values to be larger than the 2D ones in the majority of considered cases.

The present research also focuses on the influence of the third dimension on the flow behavior. For this purpose, a tank model which can be adjusted to four different widths is used. The analysis of the obtained impact pressure data is carried out by means of a classical time-domain approach, after having carried out a prior ensemble domain approach, identifying transient stages and the actual applicability of the assumption of stationarity for the impact pressure.

In addition, the influence of fluid viscosity on impact pressure values has been also investigated. To this aim experiments with water and sunflower oil, whose viscosity is 50 times larger, have been conducted. The motivation for this investigation is two-fold: on one hand, the influence of Reynolds number on nonlinear free-surface flows, and in particular on impact pressure, is a subject which is not yet well understood (see e.g. Colagrossi et al., 2013; Bouscasse et al., 2014a,b). On the other hand, it is well known that CFD codes have difficulties, due to often controlled, sometimes undesired, numerical diffusion or viscosity, to properly reproduce the physical Reynolds number (see e.g. Patankar, 1980; Morris and Monaghan, 1997).

Summarizing, the present study aims at improving the knowledge regarding the following questions:

1. How does the width of a rectangular tank affect the transient and steady state characteristics of lateral shallow depth plunging breaker impacts?
2. Similarly, what is the effect of the tank width in case of high filling ratios leading to roof impacts?
3. How are these dependencies affected by a substantial change in the Reynolds number through fluid viscosity?
4. How do these matters affect the distribution of the extreme (low probability) events?
5. Is it possible that general distributions are different while extreme ones are similar?
6. Is it possible to identify impacts, within the same forcing condition, having substantially different underlying characteristics? How do these differences reflect on the probabilistic characterization of the impact pressure?

In order to look at these matters, the paper is organized as follows: first, the experimental setup is described. Later, lateral impacts for all conditions are discussed. Subsequently, roof impacts are discussed, with particular attention given to one of the cases, for which stationary state is not achieved within the experimental time window. Some conclusions and future work threads are presented to close the paper.

2. Experimental setup

2.1. Tank model

The used tank is rectangular, with its dimensions as well as the pressure sensor array positions being shown in Fig. 1. It is a 50 times scaled down longitudinal section of a 138,000 m^3 LNG carrier membrane tank. The dimension perpendicular to the *xy*-plane (width hereinafter, *B*) can be changed by halving (0.5*X* cases), doubling (2*X*) and tripling (3*X*) the dimension (1*X*=62 mm) of the original tank (Fig. 2). The rotation center is located in the middle of the bottom side. The original tank had been the subject of research in previous papers of this series (Delorme et al., 2009; Souto-Iglesias et al., 2011) while the 3*X* geometry case was considered when developing the ensemble and time domain analyses methodology discussed in Bulian et al. (2014).

The tank models were built with 10 mm thick Plexiglas plates. The choice of the Plexiglas thickness was motivated by the resources that could be allocated for this campaign and as a convenience to obtain lighter tanks, which facilitates their manufacturing, handling and operation in the rig.

It has to be said that, as far as the authors know, neither BV nor LRS fix that thickness in their sloshing assessment procedures (LRS, 2009; Diebold, 2010). Bureau Veritas (Diebold, 2010) requires "the tank is to be enough rigid in order to be considered as rigid with respect to the measured loads", which may be interpreted in different ways. Influential works such as Lugni et al. (2006), Pistani and Thiagarajan (2012), and Song et al. (2013) do not report their model Plexiglas thickness. However, most of the tanks, in literature, for which this datum is reported are 20 mm thick (see e.g. Abrahamsen and Faltinsen, 2011; Kim et al., 2015; Loysel and Chollet, 2012) or even larger, namely 30 mm (Yung et al., 2010) or 40 mm (Lugni et al., 2010b). Interestingly, in the ISOPE benchmark, the results for our group (UPM), obtained with a 10 mm tank, did not present any significant statistical difference, which could be connected to the tank size, with respect to those of the 20 mm reference tank provided by GTT (see Figs. 14 and 16 in Loysel and Chollet, 2012).

Regarding eventual vibrations of the tank affecting the pressure peaks, following the work conducted in Bulian et al. (2014), an accelerometer was included in the sensor matrix. In addition, hammer tests were carried out with the empty tanks in order to document the natural vibration frequencies of the system. The results of the hammer tests were compared with vibrations measured during the tests, from which it was inferred that the maximum values of pressure registers were not contaminated by the strongest natural modes of the tanks.

Summarizing, we think the conclusions obtained in the paper are not affected by the Plexiglas thickness choice but, due to its interest, a future work thread about this question has been added in the conclusions section.

2.2. Rig

In the present investigation the imposed motion is harmonic with an amplitude of 4°, produced by a 1.3 kW electric actuator FESTO DNCE 63-300-BS-10-PQ (Fig. 3). The motion history is recorded by means of a digital encoder, with a precision of 0.0012°. All tests start from the same nominal initial position, horizontal, with zero angular velocity. An amplitude ramp is implemented to perform the transition between the initial rest position until the constant periodic condition. The reader is referred to Bulian et al. (2014) for details on the motion transients.

2.3. Liquids

The liquids used in the experiments (water and sunflower oil) can be considered Newtonian at standard testing conditions and their physical properties are presented in Table 1. Water properties have been taken from standard tables. On the other hand properties for the oil have been directly determined from specific experiments. Sound speed data of the fluids taken from Fontanarosa et al. (2011) is also included.

The Reynolds number can be defined based equivalently on propagation speed or on particle orbital velocity. For the lateral impacts, such velocity, U_l, can be estimated using shallow water Airy formula, taking the water depth *H* as an estimation of the order of the wave amplitude

$$U_l = \sqrt{gH} \tag{1}$$

with *g* being the gravity acceleration.

For roof impacts, the deep water solution particle velocity, with wave number *k* associated to twice the tank length *L*, can be considered; wave amplitude is assumed to be of the order of *H* (in the absence of resonance, a smaller typical amplitude based on the oscillation amplitude could be eventually chosen)

$$U_r = H\sqrt{g\,k} \tag{2}$$

Regarding typical length, *H* will be chosen for the lateral impacts (shallow water) and *L* for the roof impacts (deep water conditions).

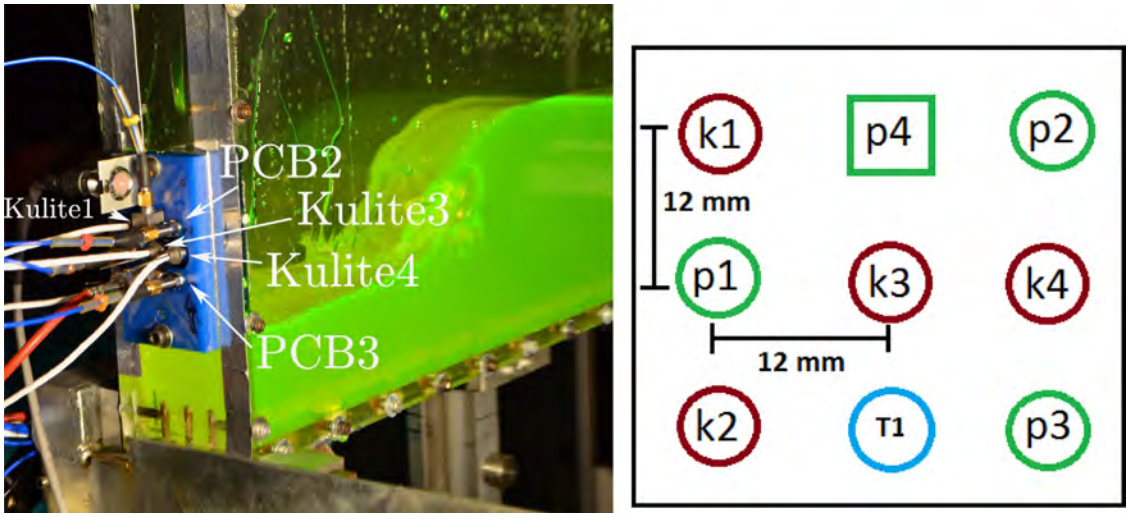

Fig. 5. Sensor array: image and configuration. Some of the sensors are labeled in the photograph so that the array orientation is clear.

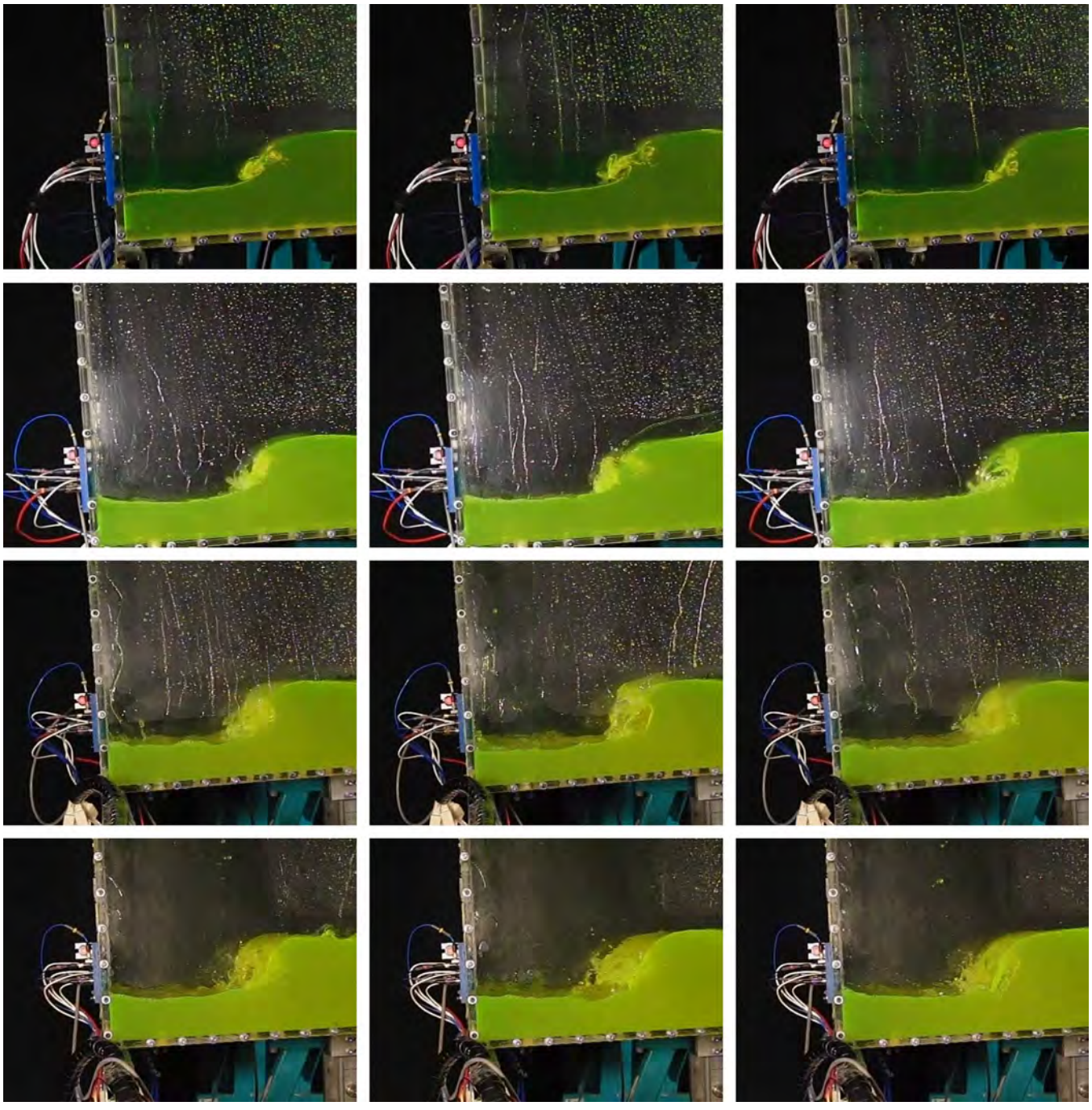

Fig. 6. Lateral impacts with water. Front view sample frames along arbitrarily chosen consecutive cycles for an arbitrarily chosen experiment. Various widths (from top to bottom rows: 0.5*X*, 1*X*, 2*X*, 3*X*). See supplementary materials at http://canal.etsin.upm.es/papers/soutoiglesiasetaloe2015/ for complete movies.

Therefore, the Reynolds number is defined as

$$Re = \begin{cases} H\sqrt{gH}/\nu & \text{for lateral impacts,} \\ HL\sqrt{gk}/\nu & \text{for roof impacts.} \end{cases} \tag{3}$$

When computed for the present campaign, the Reynolds number was found to be around 100,000 (one hundred thousand) for lateral water impacts and 2 million for roof ones. The Reynolds number for oil is around 55 times smaller than water for each case (2000 for lateral oil impacts). While the water *Re* is large enough to state that a turbulent flow will be developed, that is not so clear for lateral oil impact cases, unless turbulence is triggered by e.g. the onset of free surface breaking.

This choice of *Re*, which is the same for all tank widths, can be complemented with another non-dimensional number δ^* based on the wall boundary layer thickness δ and the tank width B

$$\delta^* = \frac{\delta}{B}. \tag{4}$$

The estimation of the boundary layer thickness, δ, is a difficult matter; Blasius flat plate laminar boundary layer or turbulent boundary layer estimations can be used. In both cases, its value will be reduced when increasing the tank width, indicating, in principle, a lower relative importance of the wall boundary layers in the bulk of the flow for wider tanks.

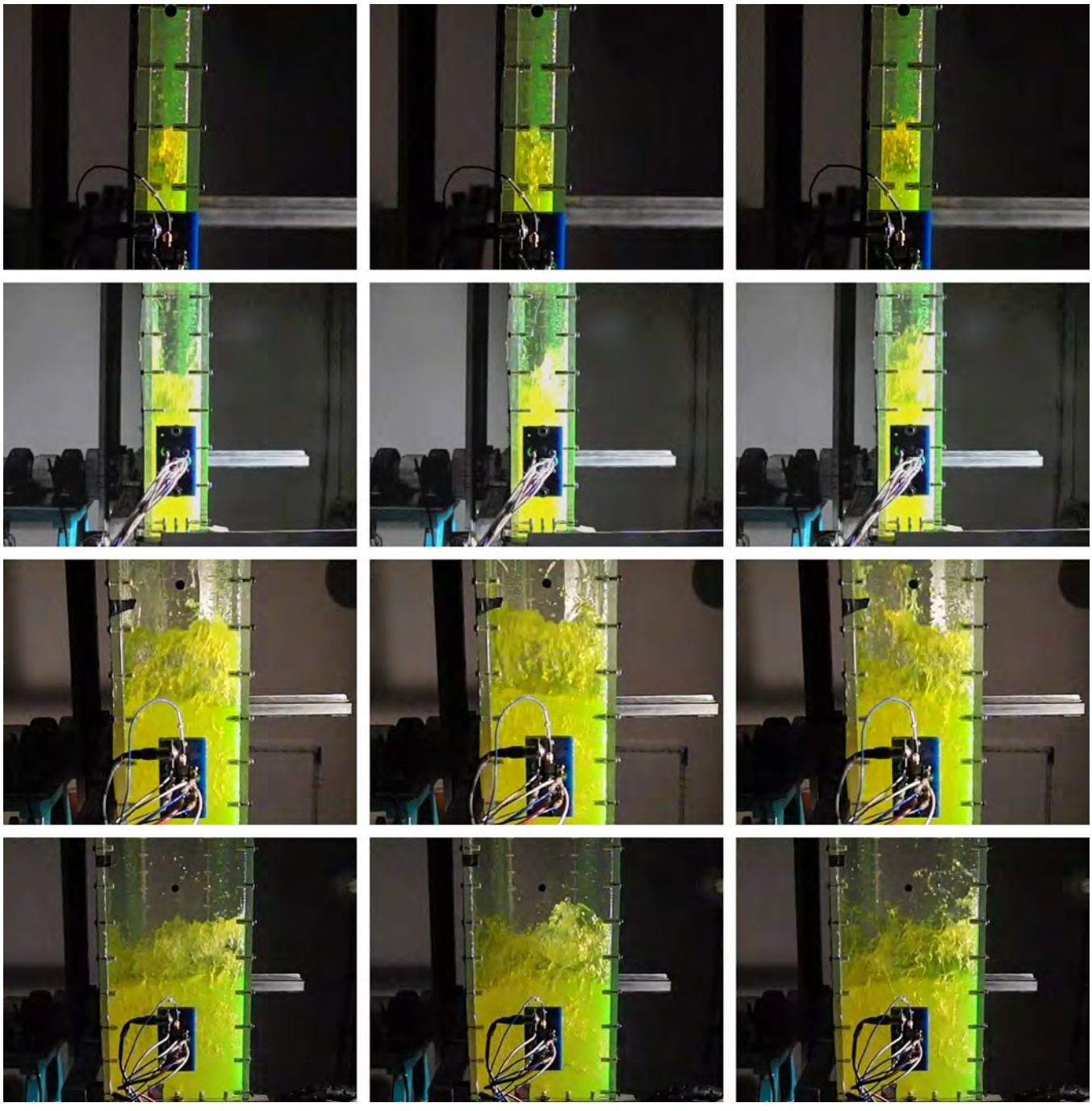

Fig. 7. Lateral impacts with water. Side view sample frames along arbitrarily chosen consecutive cycles for an arbitrarily chosen experiment. Various widths (from top to bottom rows: 0.5*X*, 1*X*, 2*X*, 3*X*). See supplementary materials at http://canal.etsin.upm.es/papers/soutoiglesiasetaloe2015/ for complete movies.

On the other hand, Weber number

$$We = \frac{\rho v^2 l}{\sigma}, \tag{5}$$

can be reasonably defined based on similar typical velocity v and distance l as *Re*. Under such assumption, its value is around 1000 for water lateral impacts and 50,000 for roof ones. Its value for oil is double that of water. In any case, it is a figure large enough to be able to confidently state that surface tension should not be responsible for the flow dynamics and more specifically for flow dynamics differences between the two liquids.

2.4. Sensors

Two types of pressure transducers have been used in the experimental campaign: Kulite piezo-resistive pressure sensors model Xtel-190(M) (Fig. 4) with 35 kPa (350 mbar) measuring range and with a 4.2 mm diameter sensing area (used previously for a dam-break flow investigation by Lobovsk et al., 2014), and PCB Piezotronics 112A21 piezo-electric with a blue 700 kPa measuring range and a 5.54 mm diameter sensing area (Fig. 4). As discussed by Loysel and Chollet (2012), significant differences can be found when, among other things, different sets of sensors are used to measure pressure peaks in sloshing flows. Kulite sensors

were statically calibrated. PCB sensors were borrowed from GTT where they had been dynamically calibrated according to their protocols (Razzak et al., 2013). Due to their different sensing method (piezo-resistive vs. piezo-electric), PCB sensors are not able to measure slow pressure variations or constant pressure levels. For this reason, on one hand they have to be dynamically calibrated and on the other hand they are able to capture the impulsive impact pressure variations but not the slow hydrostatic components that usually appear following an impact event. Considering the measuring range of both sensor types, the PCB ones will mainly support the water impacts analysis while the Kulite sensors will be the reference ones for the sunflower oil cases.

The sensors are mounted on a plate which is then attached to each of the interchangeable lateral or roof tank plates (see Fig. 5). Separation between sensors is 12 mm, the minimum achievable. Kulite sensors are labeled K1–K4 and the PCB ones P1–P3. Vibrations have been measured with one piezo-electric accelerometer (P4 in Fig. 5); model PCB Piezotronics 333B32, with a 50 g range, which is also adhered to the sensor array (see Fig. 5).

Although some authors recommend sampling rates for the pressure of 40 kHz and even higher (Repalle et al., 2010), in the present campaign 25.6 kHz sampling rate was used (this non-standard value is mandated by the piezo-electric channel card), slightly larger than 20 kHz, the one used in reference works of Lugni et al. (2006) and Graczyk and Moan (2008), heuristically demonstrated sufficient for 1/70 models, whose typical length is of the order of 1 m (Fillon et al., 2012), and recommended by Bureau Veritas (Diebold, 2010) for 1/50 scale sloshing tests. Due to the different time scaling laws of the physical processes involved during the impact events (Lafeber et al., 2012), that sampling rate ought to be adjusted for other model scales.

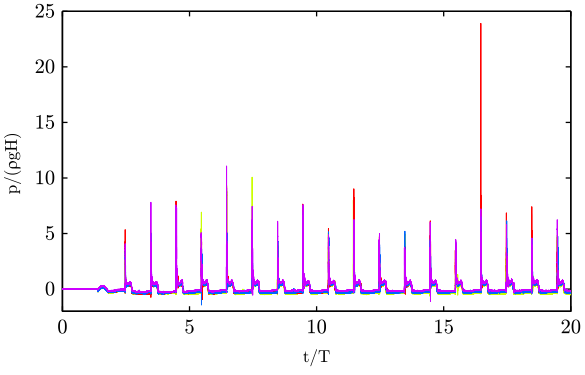

Fig. 8. Kulite sensor number 3 pressure register. Lateral water impacts. 0.5*X* tank. 4 sample experiments. First 20 oscillation periods.

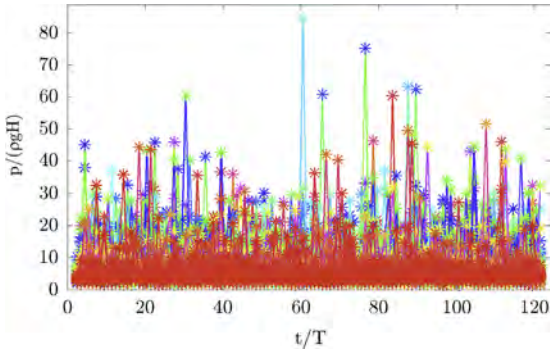

Fig. 10. Lateral impact with water. PCB number 1 sensor pressure peaks. 0.5*X* tank. 120 repetitions.

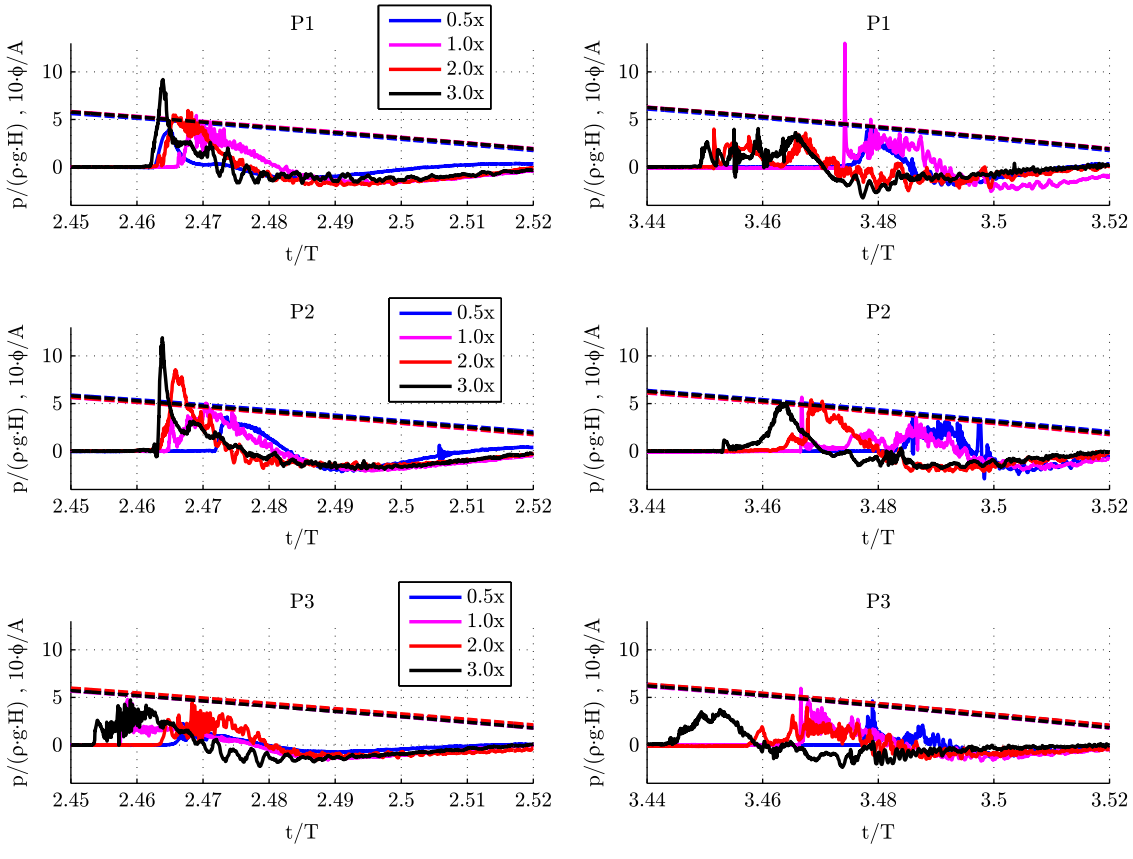

Fig. 9. Lateral impact with water. First (left) and second (right) peak pressure register (experiments with first impact pressure peak closest to the ensemble median for each width) for each PCB sensor. Dashed lines show the normalized re-scaled (10*X*) measured angular motion.

With our experimental capabilities, the underlying electronic noise introduces a reference noise level of ± 0.04 kPa which becomes the limit to our precision. Along with this, other sources of experimental uncertainties are also discussed in Souto-Iglesias et al. (2011).

Previous experimental campaigns using the same rig and similar geometrical configurations have been described by Botia-Vera et al. (2010) and have been used for CFD validation in Paik and Carrica (2014), Macià et al. (2012), Khayyer and Gotoh (2009), and Brizzolara et al. (2011). For further details on the experimental setup and a specific analysis of the uncertainties involved in the experiments, reference should be made to Souto-Iglesias et al. (2011).

3. Lateral impacts

3.1. Lateral impact with water

3.1.1. Free surface

The liquid level H for the lateral impact tests is 93 mm (18.3% filling ratio) and the center of the sensor array is placed at this level (see Fig. 1). The first sloshing period for this depth is calculated with Eq. (6), obtaining $T_1 = 1.917$ s. The period of oscillation for the water lateral tests was set to $T = 0.85T_1 = 1.629$ s for the present analysis. The first sloshing period T_1 is defined, from linear wave theory, as

$$T_1 = 2\pi \left(\sqrt{\frac{\pi g}{L} \tanh\left(\frac{\pi H}{L}\right)} \right)^{-1}, \tag{6}$$

As discussed by Delorme et al. (2009) and Bouscasse et al. (2013), larger impacts and wave elevations can be found for periods below the resonance one in shallow water conditions. Also, as discussed by Bulian et al. (2014), the impact regime changes abruptly for this filling ratio when varying the motion period. Indeed, Bulian et al. (2014) showed that, for this filling ratio and for a short window between $T/T_1 = 0.77$ and $T/T_1 = 0.80$, a transition between no-impact cases to plunging breakers that, after breaking, impact on the wall, occurs. This type of plunging breakers, impacting after breaking on the wall, are the ones that appear for a wide range of regular excitation periods above $T/T_1 = 0.80$. This is the main reason behind the period choice, selecting a value, $T/T_1 = 0.85$, which leads to this type of impact.

Using the chosen period, 120 experiments, each encompassing 120 impacts, leaving a 3-min gap between each run, were performed. In order to discuss the shape of the free surface, frames from three arbitrarily chosen consecutive cycles from an arbitrarily chosen experiment are shown in Fig. 6. As can be appreciated in these images, a significant variability in the breaking pattern is found across cycles. In addition, though the breaking types are similar for the different widths, the intensity of the splashing seems to be larger for the bigger widths. These are fully turbulent flows and therefore, even for globally periodic flows, random fluctuations occur.

Images recorded from the side where the sensor array was placed are also available (Fig. 7). They correspond to instants when the plunging breaker impacts the wall. As can be appreciated in these images, the irregularity of the free surface increases with the tank width, mainly between 0.5X, 1X and 2X. The fragmentation intensity between 2X and 3X seems similar. It can be appreciated that large air bubbles are entrapped during the impact event. It is

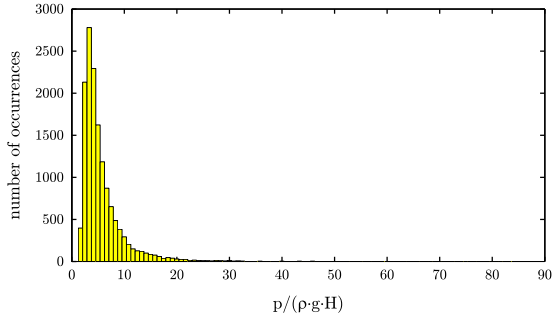

Fig. 11. Lateral impact with water: histogram of PCB sensor number 1 pressure peaks for 0.5X tank. Data from 120 repetitions, each containing 120 peaks. The isolated large peaks in Fig. 10 are responsible for the extremely long tail of the distribution.

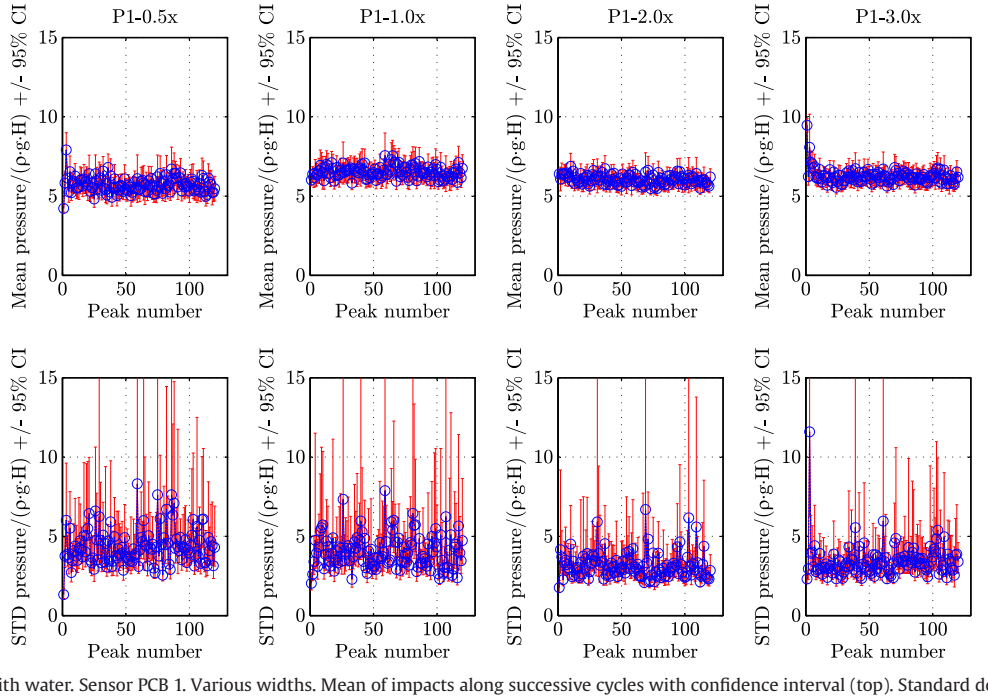

Fig. 12. Lateral impact with water. Sensor PCB 1. Various widths. Mean of impacts along successive cycles with confidence interval (top). Standard deviation with confidence interval (bottom).

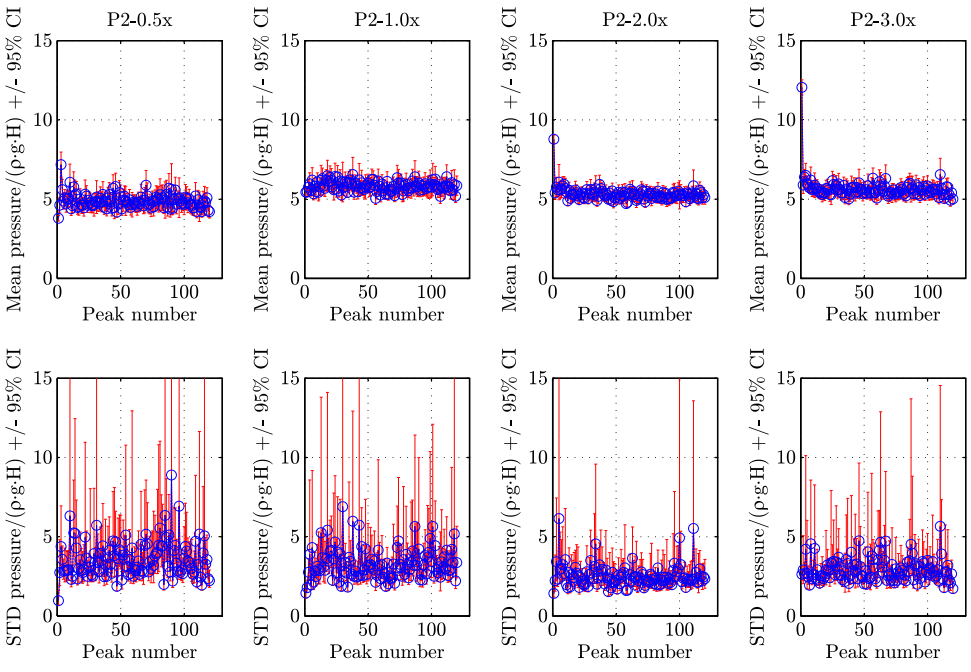

Fig. 13. Lateral impact with water. Sensor PCB 2. Various widths. Mean of impacts along successive cycles with confidence interval (top). Standard deviation with confidence interval (bottom).

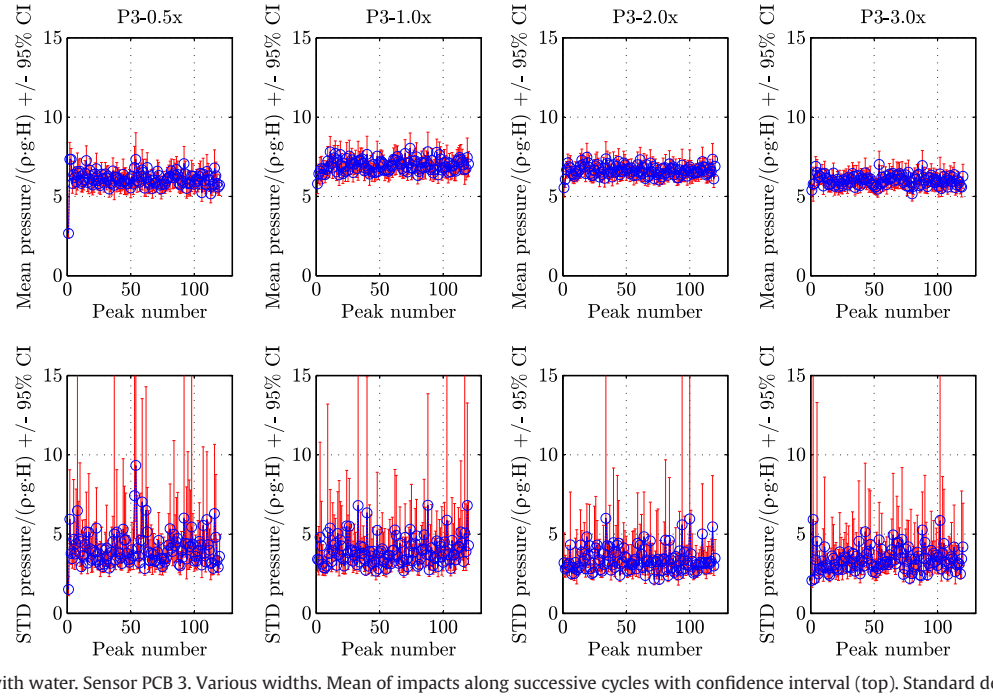

Fig. 14. Lateral impact with water. Sensor PCB 3. Various widths. Mean of impacts along successive cycles with confidence interval (top). Standard deviation with confidence interval (bottom).

well known that the presence of air bubbles in the fluid can have a substantial influence on the pressure field either because compression–expansion cycles are formed or due to local modification of the sound speed in the aerated fluid (see e.g. Lugni et al., 2006, 2010a; Topliss, 1993; Abrahamsen and Faltinsen, 2011; Hattori et al., 1994).

3.1.2. *Pressure time histories*

In Fig. 8, the pressure registered during the first 20 cycles by the K3 sensor is plotted for four arbitrarily chosen example experiments. As can be seen, the impact pressure events are characterized by the well-known "church roof shape" (Peregrine, 2003). It is remarkable that, in some of the cases, the impact pressure is around 25 times the hydrostatic pressure at the bottom of the tank. Some negative pressure values can be appreciated; the ones corresponding to the first impact is due to electronic noise generated during the transition of the sensor from dry to wet (Bulian et al., 2014; Kim et al., 2015; Pistani and Thiagarajan, 2012). The ones in subsequent impacts are due to effective negative pressures prior to secondary impacts or during bubble entrapment.

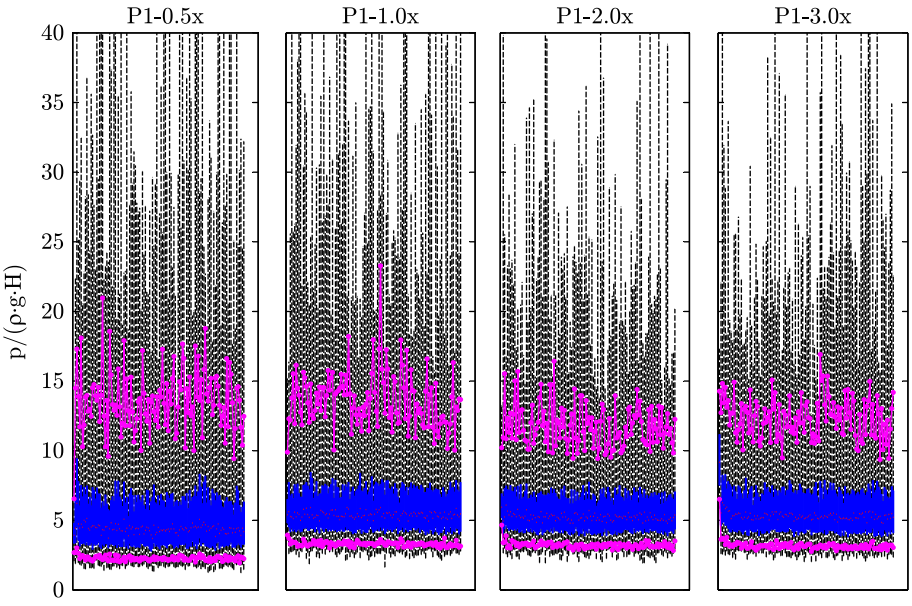

Fig. 15. Lateral impact with water. Sensor PCB 1. Various widths. Box plot with minimum, 5%, 25%, 50% (median), 75% and 95% percentiles, and maximum, for each peak. Peak number on the *x*-axis.

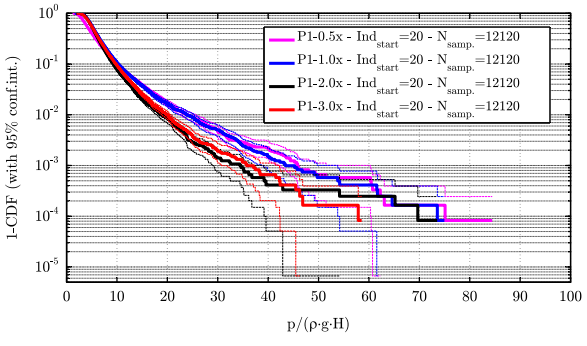

Fig. 16. Lateral impact with water. Sensor PCB 1. Various widths. Exceedance probability graph.

From the previously mentioned figure, it can be appreciated that the pressure peak values show a certain random behavior, which is a consequence of the multiphase turbulent flow described in previous paragraphs. To statistically characterize such a behavior, 120 experiments containing each 120 cycles (and thus peaks) have been carried out for each of the cases considered in this paper. This approach allows for the investigation of the transient and stationary characteristics of the pressure peaks, both in time and ensemble domain (Bulian et al., 2014).

In the left panels of Fig. 9, time histories of peak events 1 and 2 of the experiments whose peak 1 is, for each PCB sensor (see Fig. 5 for sensor positions), closest to the median, are presented for the four widths. It must be borne in mind that PCB sensors, as discussed in Section 2, cannot record the slow varying pressure components, such as the ones taking place just after impact, being the reason for the large difference between Figs. 8 and 9 regarding the shape of the pressure time history immediately after the peak. Looking at Fig. 9, it is noticeable that for peak 1 and sensors P1 and P2, the 0.5*X* peak displays a consistent lower pressure than the rest, followed by 1*X*, etc. Sensor P3 shows a more complex behavior, exemplified by the large amount of high frequency components in the 3*X* width registers.

Time histories of event 2 are presented for these very same experiments in right panels of Fig. 9. It has to be borne in mind that, while the first peaks are special in the sense that they represent peaks closest to the ensemble median, this is not the case for the second impacts of the same runs. While it is not possible to draw any conclusion from the direct comparison of the impact pressure for the example second impacts (as explained, these are "non-special" cases), it is nevertheless possible to identify a tendency for the impact to occur earlier when the tank width is larger. This might be associated with an increased effect of the viscous boundary layer at smaller widths.

3.1.3. *Statistics*

It is important that the experiments are conducted in extremely similar conditions so that the pressure values for each of the peaks can be considered a realization of the same random process, with, hence, the same probabilistic distribution. This aspect has been dealt with by trying to control all those variables affecting the overall boundary conditions of the problem. As an example, the PCB1 sensor peaks of the 120 repeated experiments for the 0.5*X* width, are plotted in Fig. 10. Although non-dimensional pressure of most events falls around 10, quite isolated low probability large pressure value events are evident from the figure. This isolated values are reflected in the long tail of the histogram of these values displayed in Fig. 11.

Using a harmonic motion allows for an impact in every cycle to occur, and it is easy to identify them due to the good repeatability of the motion. Regarding their statistics, the ensemble mean of the peak pressure for all experiments in every impact event, with its confidence interval (see Bulian et al., 2014) for details on how confidence intervals are estimated), is plotted in Figs. 12–14 for sensors P1, P2 and P3 for all tanks (see Fig. 5 with sensor positions). The evolution of the mean is inspected in these figures while the median and percentiles will later be discussed. A short transient in the initial peaks is observed in all cases. As can be appreciated, there is no substantial difference in the steady state mean across the tanks of different widths.

The standard deviation, with confidence interval estimated with the "Adjusted Degrees of Freedom" method (see again Bulian et al., 2014 for details), is presented in the bottom plots. It is interesting to notice that the values of the ensemble standard deviation are quite similar for all widths, but a larger dispersion is visible for smaller widths. Considering these facts, a large

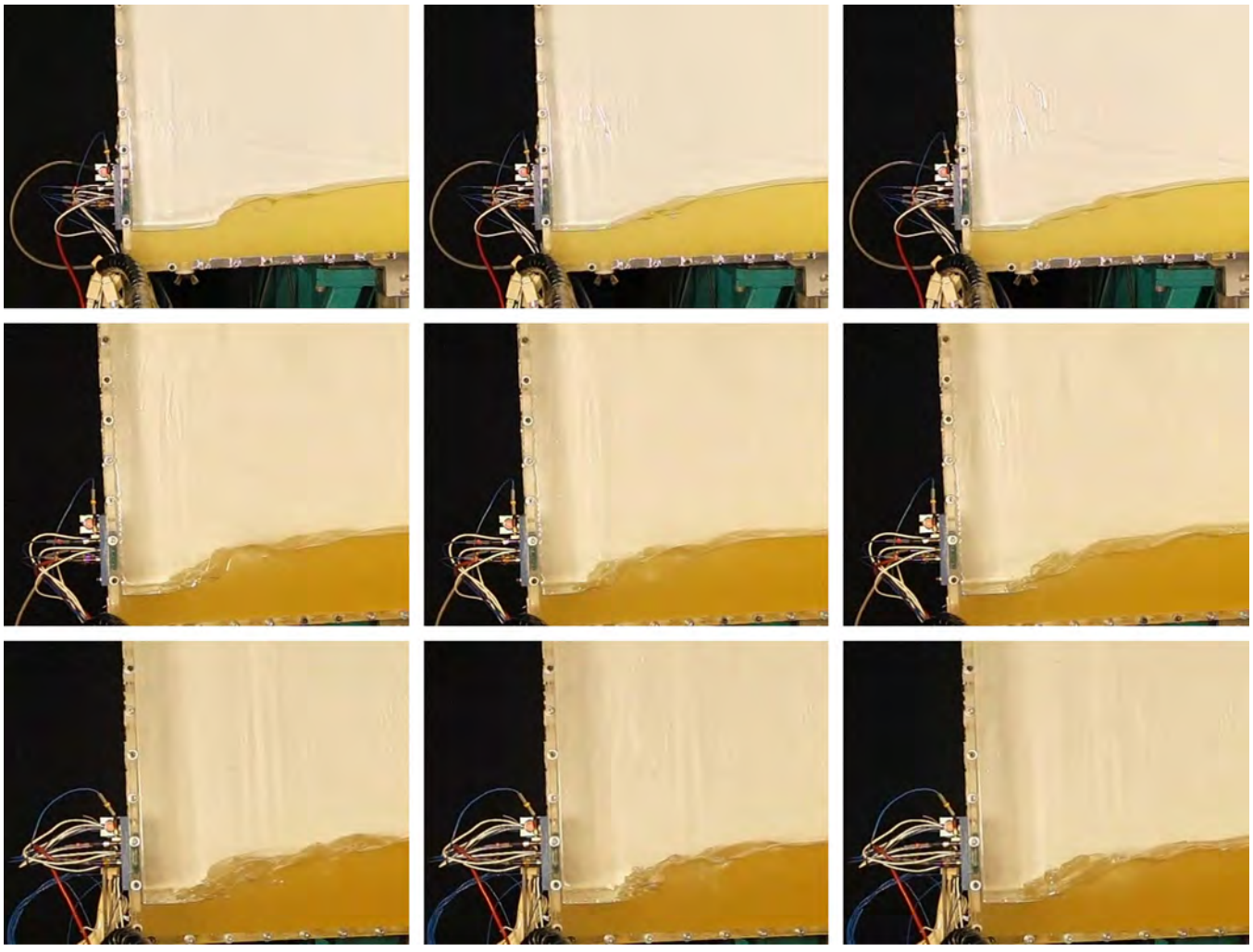

Fig. 17. Lateral impacts with oil. Front view sample frames along arbitrarily chosen consecutive cycles for an arbitrarily chosen experiment. Various widths (from top to bottom rows: 1*X*, 2*X*, 3*X*). See supplementary materials at http://canal.etsin.upm.es/papers/soutoiglesiasetaloe2015/ for complete movies.

Fig. 18. Lateral impact with oil. 1*X*. Free surface details.

influence of width on peaks statistics seems to currently not be present.

The statistics of the peaks can be looked at in more detail by presenting, for each peak number, a box plot with minimum, 5%, 25%, 50% (median), 75% and 95% percentiles, and maximum. This is done for sensor PCB 1, in Fig. 15 (other sensors display similar outcomes). The 95% threshold is larger for 0.5*X* and 1*X* and the distributions become more compressed for 2*X* and 3*X*. The median is, on the other hand, slightly smaller for 0.5*X* and remains similar for the other widths. Differences are not large and it seems the width influence on the distribution is not substantial. However, there is a tendency for the smaller widths to be associated with wider distributions. This is more evident especially when looking at the size of the interval between the 5% and 95% percentile levels.

Removing the transients from the analysis (20 peaks in each case), and assuming that, for each tank width, all peaks share the same distribution, empirical exceedance probability graphs can be obtained for each width for different sensors (approximately 12,000 observations). The graphs corresponding to PCB 1 are presented in Fig. 16. For large probability levels, 0.5*X* shows slightly lower pressure values but as we move to the low probability region, the trend is inverted, with 1*X* and 0.5*X* displaying the largest pressures. These characteristics are, of course, in line with the observations made with respect to the dispersion of data in the ensemble domain analysis in Fig. 15. This is a remarkable feature, consistent with the findings of Schreier and Mehl (2012) during the ISOPE benchmark, who looked at this matter for translational motion roof impacts. It suggests that the kinetic energy may be partially transferred to transversal modes for wider tanks, something which reduces the normal pressure. This trend will be further inspected when analyzing roof impacts.

3.2. *Lateral impact with oil*

3.2.1. *Free surface*

The physical properties of the oil used in the experiments are shown in Table 1. After a screening of forcing periods, the period of

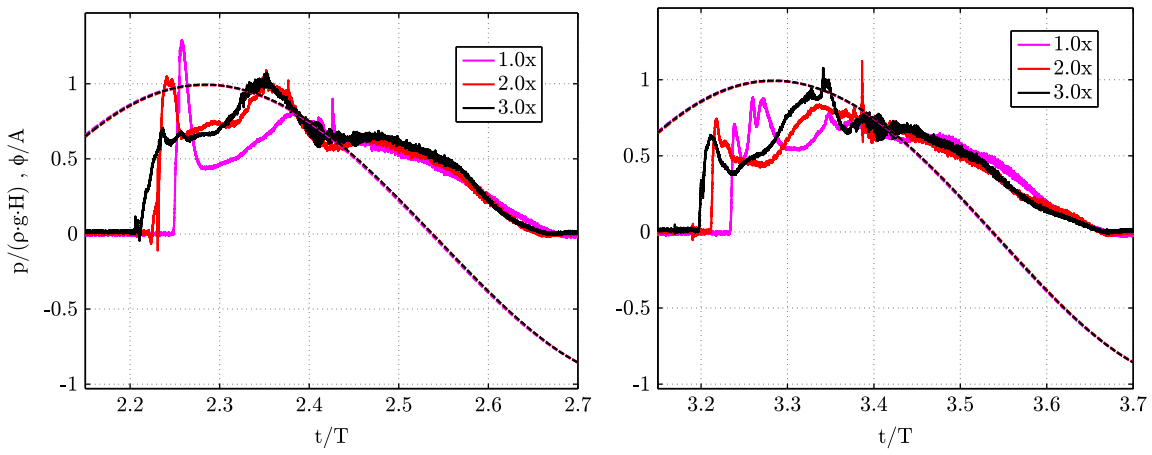

Fig. 19. Lateral impacts with oil. First (left) and second (right) peak pressure register for Kulite 3 sensor (experiments with first impact pressure peak closest to the ensemble median for each width). Dashed lines show the normalized measured angular motion.

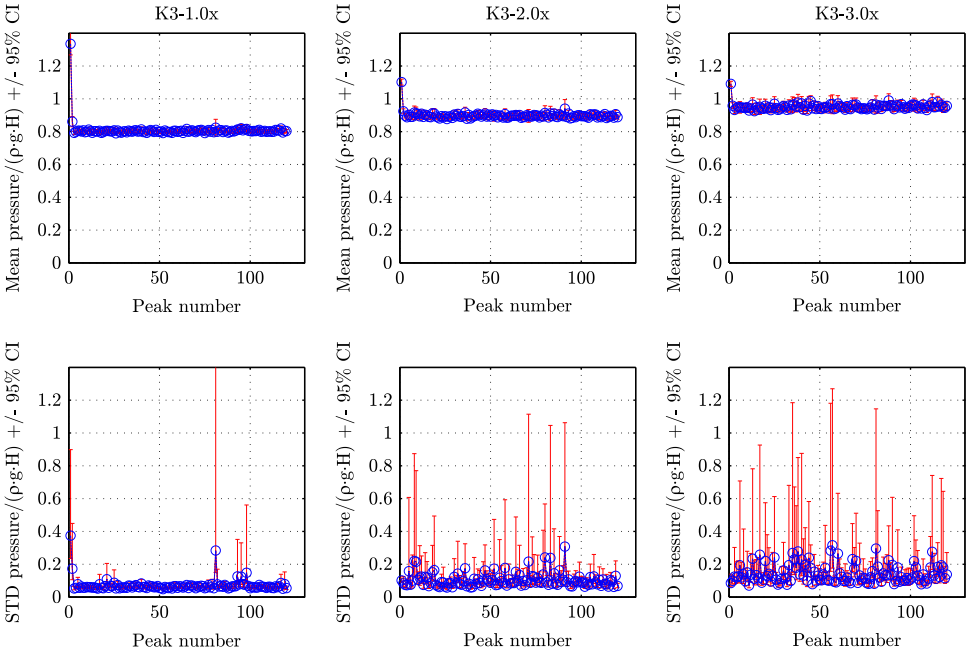

Fig. 20. Lateral impact with oil. Sensor Kulite 3. Various widths. Mean of impacts along successive cycles with confidence interval (top). Standard deviation with confidence interval (bottom).

oscillation for the oil lateral tests was set to $1.15T_1 = 2.205$ s. For the same period like water, impact does not take place for oil. For the chosen period, a spilling breaker is found, introducing an interesting new type of impact in the analysis.

Independently of the period choice, the dynamics is expected to significantly differ from water's, due to the reduction in Reynolds number arising from the increase in kinematic viscosity. Such larger viscosity induces a significant thickening of the boundary layers, both at the free surface (Liu and Davis, 1977; Colagrossi et al., 2013) and at the solid boundaries, the latter being reflected in a larger relative boundary layer thickness ratio δ^* (see Eq. (4)).

In Fig. 17, a sequence of images corresponding to consecutive sample events prior to impact is shown. 0.5*X* case is omitted in the analysis due to the fact that some problems were detected with the acquired pressure data during the data processing phase. For 1*X*, some 3D effects appear with a central structure formed at the wave front. This can be better appreciated in the dedicated image presented in Fig. 18, where fascinating close to breaking patterns can be observed. For 2*X* and 3*X*, a mild spilling breaking event occurs, whose dynamics does not seem to vary much between 2*X* and 3*X*.

3.2.2. *Pressure time histories*

Let us focus now on a set of representative pressure time histories: in Fig. 19, time histories of events 1 and 2 in the experiments whose peak 1 is, for Kulite 3 sensor (see Fig. 5 for sensor position), closest to the median, are presented for the four widths. Kulite sensors have been chosen for the analysis of oil cases since their acquisition range better fits the lower than water pressure values found for these cases.

As can be seen in the left panel of Fig. 19, peak 1 is consistently larger for the 1*X* width tank, with 2*X* coming next and 3*X* being the lowest. In addition, it can also be observed that the shape of the pressure time history for the first impact is different when comparing the three widths. Although in Fig. 19 only three representative cases are reported, such change in shape is

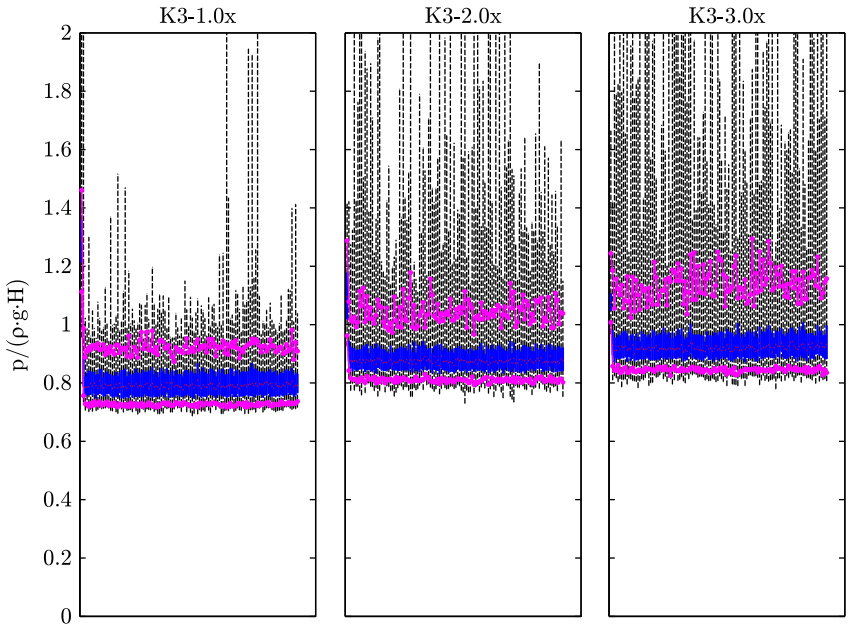

Fig. 21. Lateral impacts with oil. Sensor Kulite 3. Various widths. Box plot with minimum, 5%, 25%, 50% (median), 75% and 95% percentiles, and maximum, for each peak. Peak number on the *x*-axis.

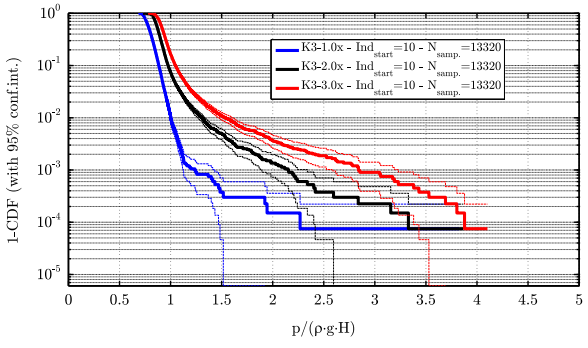

Fig. 22. Lateral impacts with oil. Sensor K3. Various widths. Exceedance probability graph.

consistently reproduced with the repetitions of the experiments for each width. Moreover and also in this case (lateral impact with oil), a trend for the impacts to occur earlier in case of larger widths is clearly visible, which could be a consequence of viscous boundary layer effects.

For these same experiments the second impact is also shown in the right panel of Fig. 19. Notice that these are "non-special" cases, something which makes meaningless a one-to-one comparison of the impact pressure peaks. However, the trend towards earlier impacts for larger widths is clearly noticeable.

3.2.3. *Statistics*

Analogously to the water case, in Fig. 20 the ensemble mean of the peak pressure for all experiments in every impact event for the Kulite 3 sensor, located at the array center (see Fig. 5 for sensor position), is presented for oil. Confidence intervals are included in the figure.

A very short transient in the initial peaks is observed in all cases. As can be appreciated, there is a slight increase in the mean as the widths increase. Though not strictly comparable with the water case, the mean pressure values are around one order of magnitude smaller for this case. Regarding the repeatability of the data, it is very large, something which is reflected in the low values of the standard deviation. However, for increasing widths, the confidence interval of the standard deviation increases, which is a consequence of a larger data scattering for larger width tanks.

The statistics of the peaks are analyzed in more detail by presenting, for each peak number, a box plot with minimum, 5%, 25%, 50% (median), 75% and 95% percentiles, and maximum. This is done, for sensor K3, in Fig. 21 (other sensors display similar outcomes). The 95% percentile pressure is larger for 1*X* in the transient but in the steady state it is 3*X* that shows the largest 95% percentile pressure. The median displays a similar trend to the mean from the previous figure. The variation of the 95% level is larger for the 2*X* and 3*X*, compared to 1*X*, consistently with the trends in the standard deviation confidence intervals. Therefore, moving from the smaller width ($1\times$) to the largest width ($3\times$), the steady state ensemble distribution tends to shift towards larger pressures and to become broader.

After having analyzed the main characteristics of the ensemble distribution of the impact pressure, it is then possible to move to the analysis of low probability levels. Removing the transients from the analysis (10 peaks in each case), empirical exceedance probability graphs can be obtained for each tank width for sensor K3. They are presented in Fig. 22. The low probability levels show a consistent increase of the pressure with the tank width. This is very noticeable, for instance, at probability levels of 10^{-3}, for which the confidence intervals of the cumulative distribution functions (cdfs) are still small enough to allow for a statistically meaningful comparison. To summarize, the width of the tank has been found to significantly influence the peak pressure values. Therefore, simulating these flows requires modeling 3D effects such as those corresponding to the boundary layers in the front and back plates of the tank.

4. Roof impacts

4.1. *Roof impact with water*

4.1.1. *Free surface*

Roof impacts are quite relevant in the industry due to the tank roof being often less reinforced than the bottom part and hence,

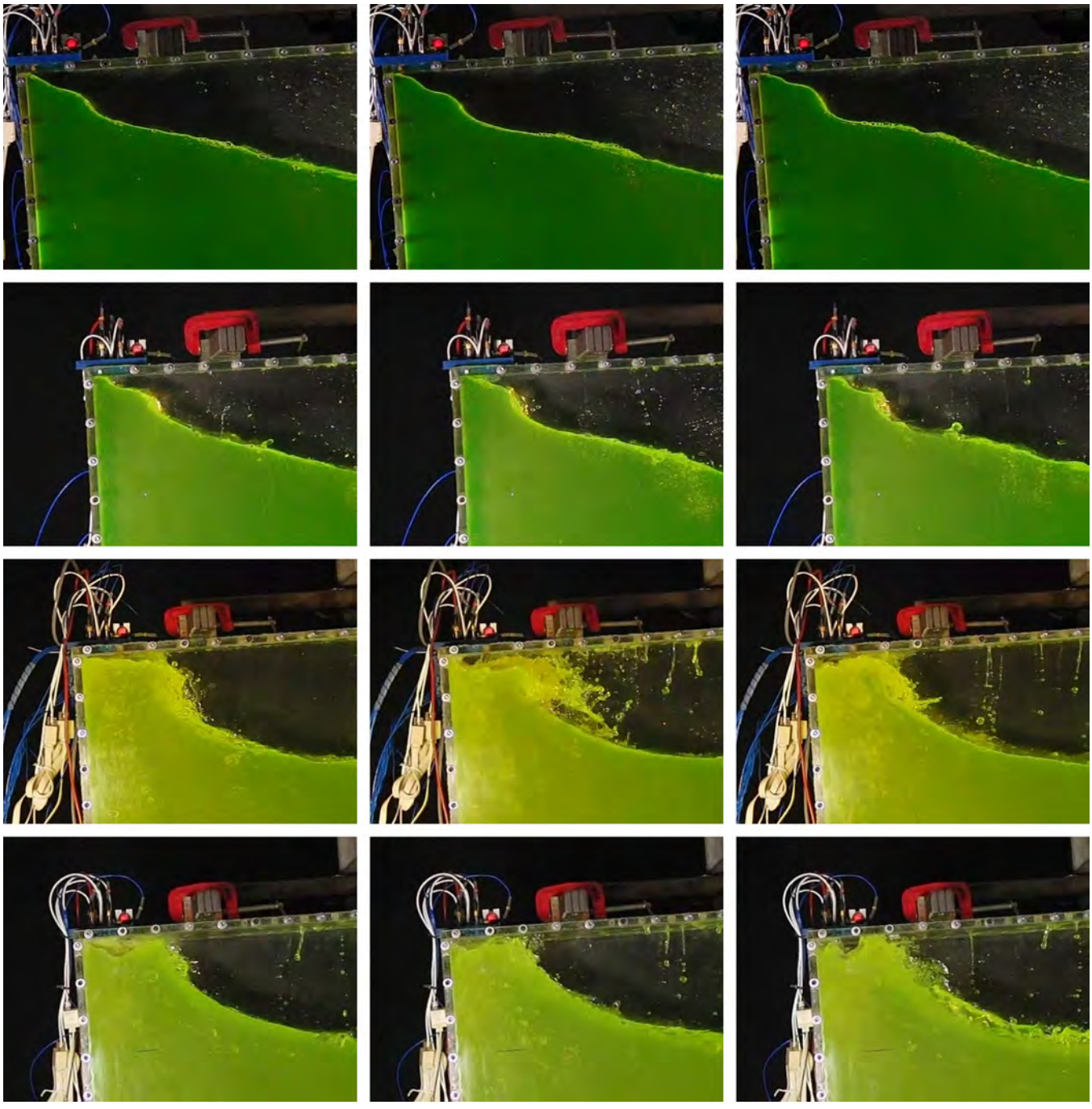

Fig. 23. Roof impacts with water. Front view sample frames along arbitrarily chosen consecutive cycles for an arbitrarily chosen experiment. Various widths (from top to bottom rows: 0.5*X*, 1*X*, 2*X*, 3*X*). See supplementary materials at http://canal.etsin.upm.es/papers/soutoiglesiasetaloe2015/ for complete movies.

subject to higher risks for the same order of impact pressure values. In order to obtain a liquid dynamics leading to roof impacts, the liquid level for this set of experiments is set to a 70% filling ratio (355.6 mm). Such a filling level corresponds to a first linear mode with period $T_1 = 1.167$ s. The period of oscillation has been chosen as $T = 1.15 \cdot T_1 = 1.343$ s, with roof impacts taking place in each cycle. In this configuration, neither overturning nor breaking waves are generated. This period was chosen in order to reduce the number of saturation events for the Kulite sensor set. Akin to lateral impacts, 120 experiments were run each encompassing 120 peaks, leaving a 3-min gap between each run.

Regarding flow discussion (Fig. 23), the free surface remains single-valued and moves up against the roof. Air is hardly entrapped during the impact events for 0.5*X* and 1*X*, with the free surface progressively approaching the roof. This is not the case for 2*X* and 3*X*, with direct flat impacts on the roof, including air entrapment. As discussed in Section 3.1, the presence of air bubbles in the fluid is known to have a substantial influence on the pressure field.

The influence of the tank width on the flow, represented by the variations in the free surface shape along three arbitrarily chosen consecutive cycles, increases dramatically with the tank width. It is

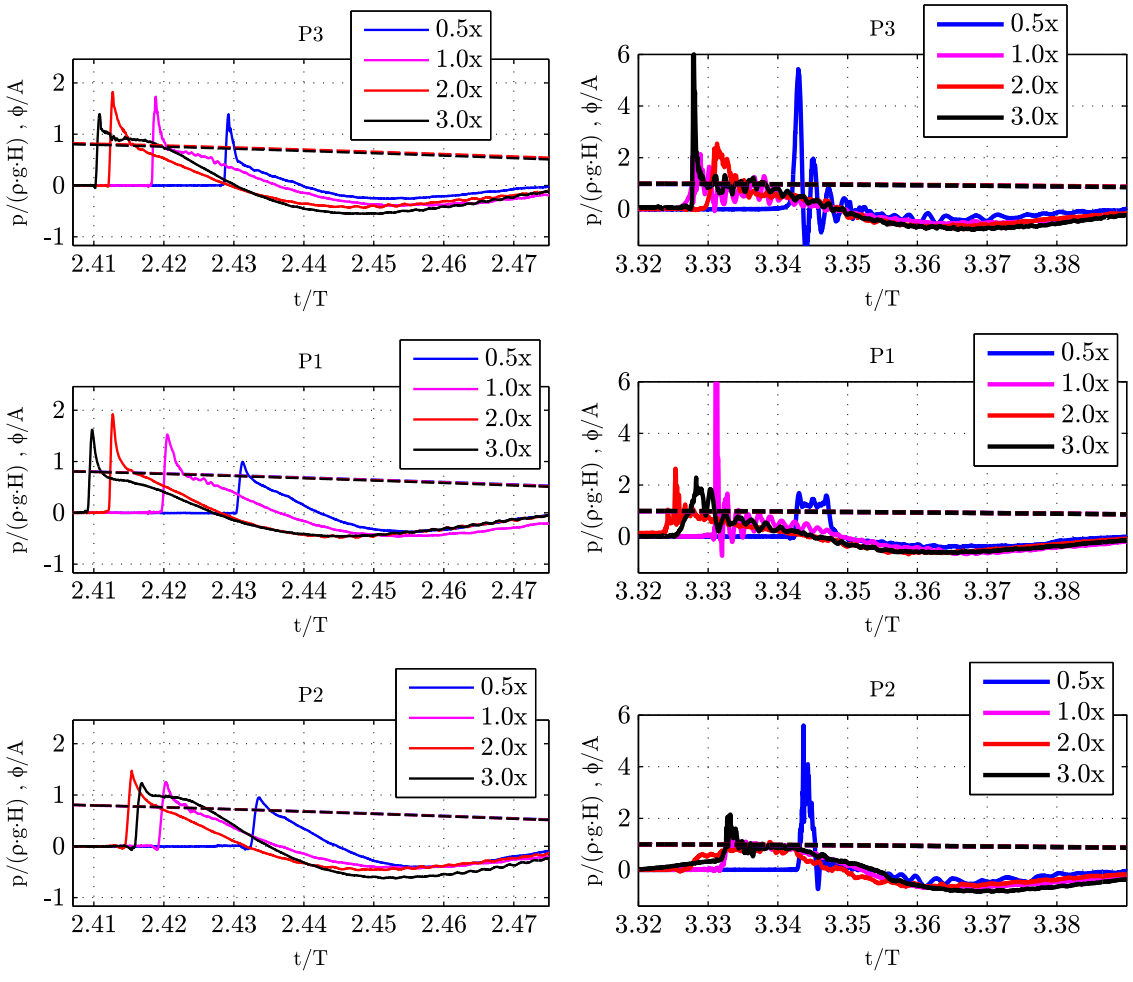

Fig. 24. Roof impacts with water. First (left panels) and second (right panels) peak pressure registers for each PCB sensor (experiments with first impact pressure peak closest to the ensemble median for each width). Dashed lines show the normalized measured angular motion.

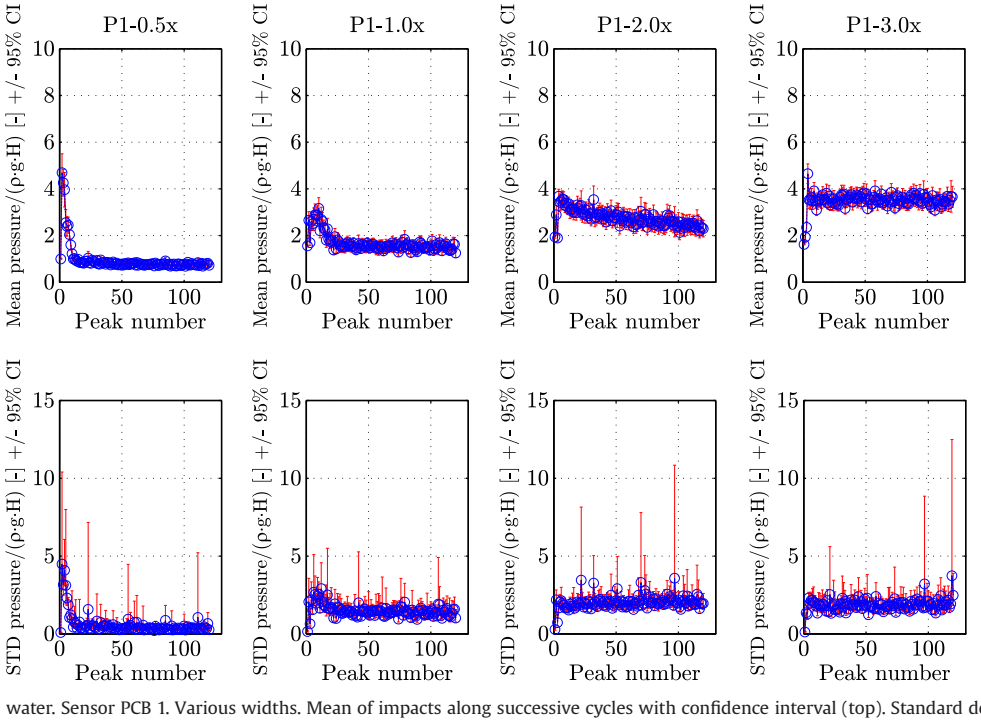

Fig. 25. Roof impact with water. Sensor PCB 1. Various widths. Mean of impacts along successive cycles with confidence interval (top). Standard deviation with confidence interval (bottom).

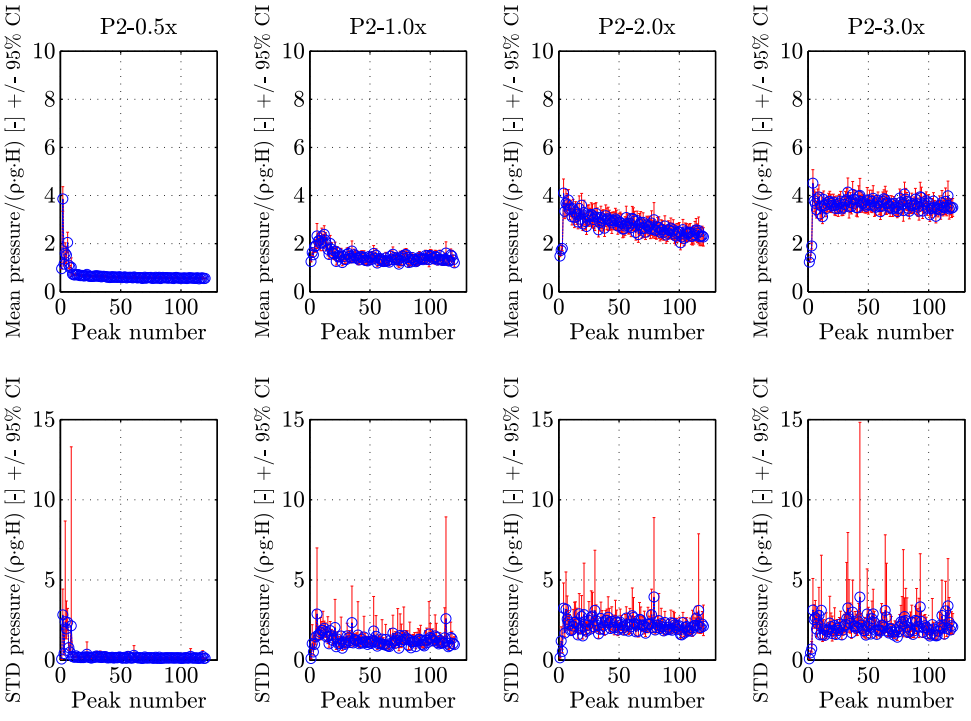

Fig. 26. Roof impacts with water. Sensor PCB 2. Various widths. Mean of impacts along successive cycles with confidence interval (top). Standard deviation with confidence interval (bottom).

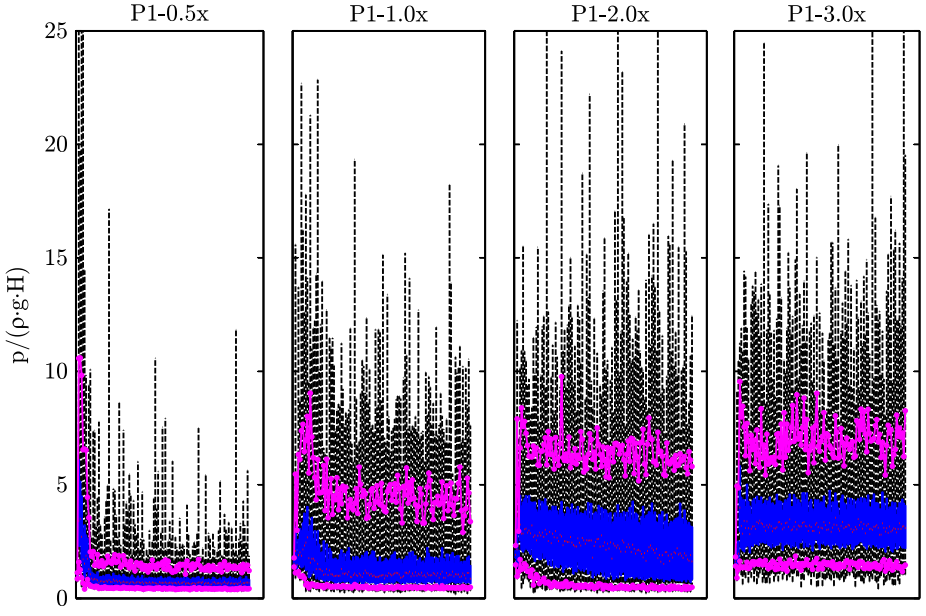

Fig. 27. Roof impacts with water. Sensor PCB 1. Various widths. Box plot with minimum, 5%, 25%, 50% (median), 75% and 95% percentiles, and maximum, for each peak. Peak number on the *x*-axis.

noticeable that significant free surface instabilities develop for cases 2*X* and 3*X*.

4.1.2. *Pressure time histories*

In Fig. 24, time histories around peaks 1 and 2 of the experiments whose peak 1 is, for each sensor, closest to the median, are presented for the four widths. For 2*X* and 3*X* cases, peak number one happens slightly earlier than 0.5*X* and 1*X*. This can be attributed to the fact that they feel the drag, due to the boundary layers developing on the front and back plates of the tank, proportionally less. Apart from that, and as we move from the corner towards the center of the tank along the upper plate, the size of the first peak is comparable for sensor 3 (closest to the corner) for all tanks and slightly lower for sensors P1 and P2.

The time history for event 2 is presented for these very same experiments. For sensor P3, the 0.5X peak seems to correspond to the entrapment of a bubble while different dynamics are present

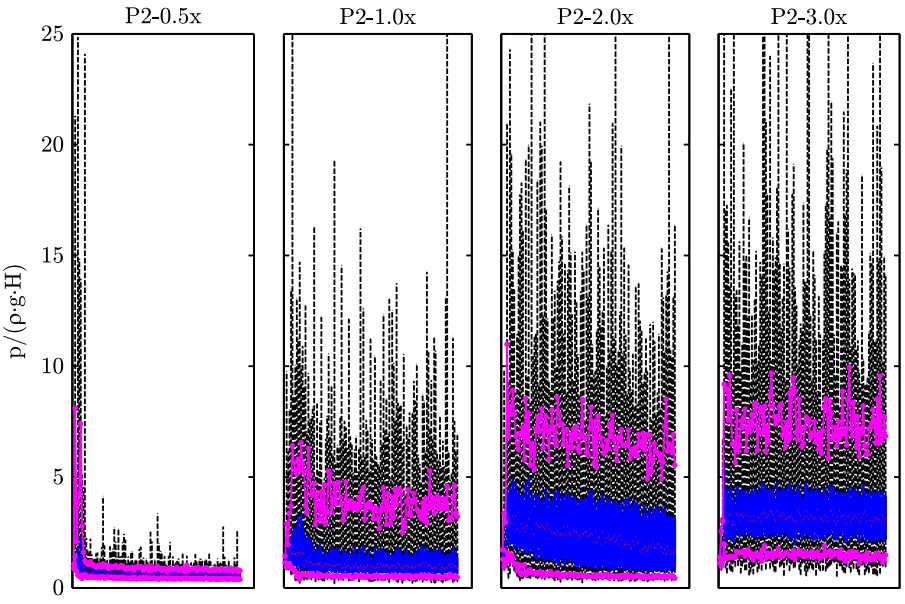

Fig. 28. Roof impacts with water. Sensor PCB 2. Various widths. Box plot with minimum, 5%, 25%, 50% (median), 75% and 95% percentiles, and maximum, for each peak. Peak number on the *x*-axis.

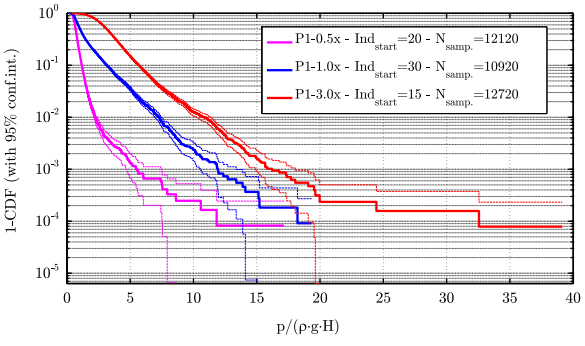

Fig. 29. Roof impacts with water. Sensor PCB 1. Various widths. Exceedance probability graph.

for the same sensor in the experiments corresponding to the other widths.

4.1.3. Statistics

In Fig. 25 (upper plots), the ensemble mean impact pressure for each impact, together with associated confidence interval, is plotted for sensor P1 (PCB 1) for all tank widths. As can be appreciated from Fig. 5, sensor P1 is in the mid transversal line of the array. The transient takes around 20 cycles for 0.5*X*, 30 for 1*X*, 15 for 3*X* and no steady state is found for 2*X*. Regarding the steady state values, the mean values are much smaller for 0.5*X* than 1*X*, while the mean value for 3*X* is around 50–100% larger.

Standard deviation is presented in the bottom plots and the transients are reflected in its value and confidence intervals. The standard deviation in steady state is very low for 0.5*X* (largest repeatability), grows for 1*X* and remains very similar for 2 and 3*X*. Therefore, it seems that for the roof impacts there is a substantial influence on the peaks of the flow variations induced by the width changes in the tank, mainly between the smallest widths and the 3*X* one.

Mean values in the ensemble domain are plotted in Fig. 26 for sensor P2 (PCB 2), which, compared to sensor P1, is positioned further away from the tank corner. The trends of P1 for the 0.5*X* configuration are maintained. With regard to the other widths, there is a growth from 1*X* to 2*X* and 3*X*. Again, no steady state is found for the 2*X* case, which is a remarkable feature.

The statistics of the peaks can be looked at in more detail by presenting for each peak a box plot with minimum, 5%, 25%, 50% (median), 75% and 95% percentiles, and maximum, for each peak. This is done first for sensor PCB 1 in Fig. 27 and for sensor PCB 2 in Fig. 28. The transients are reflected in both figures. The remarkable difference between both sensors for the 0.5*X* case is also noticeable.

Removing the transients from the analysis and assuming that in each tank width all impacts share the same distribution (2*X* data is discarded since no stationary state is achieved), empirical exceedance probability graphs can be obtained for each tank width for different sensors (approximately 11,000–13,000 observations). The graphs corresponding to PCB 1 are presented in Fig. 29. The trends observed in the ensemble domain analysis are confirmed when looking at the low probability levels, for which the 3*X* width tank has the largest values. It is remarkable however to notice that the divergence between 0.5*X* and 1*X* stops increasing when going to such low probability levels.

To summarize, it seems that, overall, the larger the width, the larger the pressures. This result challenges, somehow, previous published research by Schreier and Mehl (2012), who found an opposite behavior (i.e. a decrease of roof impact pressure in case of a wider tank compared with a narrower tank). It is however important to keep in mind that a direct comparison between experimental results presented herein with those from Schreier and Mehl (2012) is not possible, due to the differences in the experimental configuration: angular vs. translational motion, moderate amplitude vs. large amplitude motions, different tuning factors, etc. Nevertheless, the qualitatively different outcomes found herein and in Schreier and Mehl (2012) highlight the importance of the width factor, and in general of three-dimensional effects, not only from a practical (industrial) point of view, but also from and academic research point of view.

4.2. Roof impact with oil

4.2.1. Free surface

For oil, the same period as for roof water cases is used, $T = 1.15 \cdot T_1 = 1.343$ s. A sequence of images for each width is

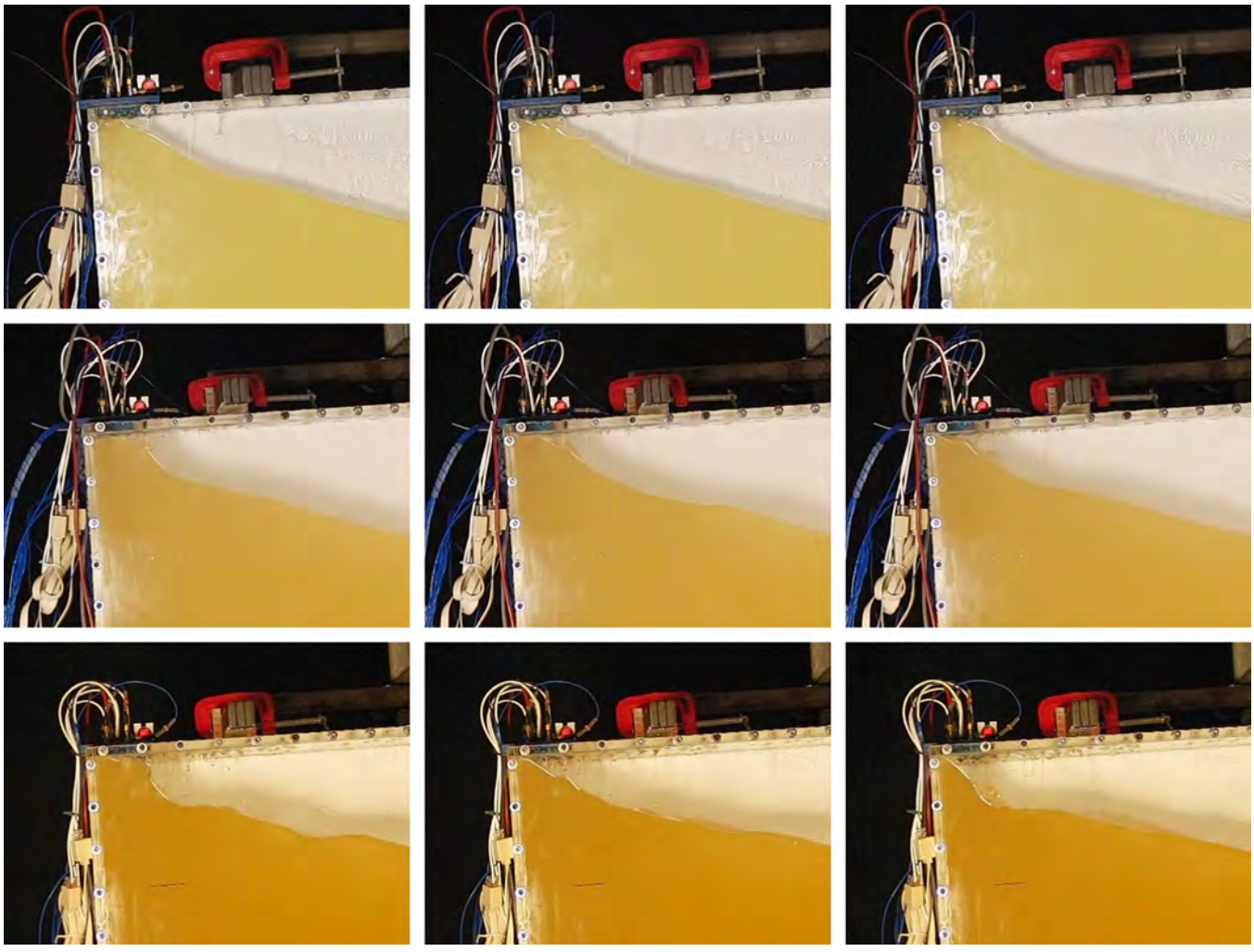

Fig. 30. Roof impacts with oil. Front view sample frames along arbitrarily chosen consecutive cycles for an arbitrarily chosen experiment. Various widths (from top to bottom rows: 1*X*, 2*X*, 3*X*). See supplementary materials at http://canal.etsin.upm.es/papers/soutoiglesiasetaloe2015/ for complete movies.

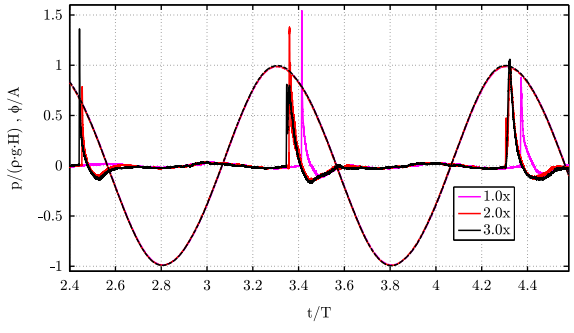

Fig. 31. Roof impacts with oil. Register for experiments with impact pressure peaks at $t/T \sim 3.4$, for Kulite 3 sensor, closest to the ensemble median for each width. Dashed lines show the normalized measured angular motion.

shown in Fig. 30. The 0.5*X* case is not presented due to some acquisition issues which were identified in the post-processing stage, when repeating the experiments could not be considered. The dynamics are overall similar to the water roof impact case. Variability across cycles in the free surface takes place for 2*X* and 3*X* but with much lower development of instabilities at the free surface than for the water case. No large effect due to a width increase can be appreciated.

4.2.2. *Pressure time histories*

In this case, for 1*X* the first impact occurs one cycle later than for 2*X* and 3*X*. For this reason, representative time histories have been chosen as those with peak impact pressure closest to ensemble median for the impact at $t/T \sim 3.4$, for Kulite 3 sensor (see Fig. 5 for sensor position). These pressure time histories are displayed in Fig. 31. The delay of 1*X* impacts compared to 2*X* and 3*X* is noticeable.

4.2.3. *Statistics*

In Fig. 32, the ensemble mean of impacts along successive cycles is plotted for sensor K3 for all tank widths (see Fig. 5 for sensor positions). A steady state seems to be achieved for all widths. The steady state mean value is around one for 1*X*, doubles to 2 in 2*X* and then, surprisingly, falls to 0.5 for 3*X*. Looking at the flow or at the time histories does not seem to indicate the reason for such pressure values, which were double checked.

The statistics of the peaks can be looked at in more detail by presenting, for each peak, a box plot with minimum, 5%, 25%, 50% (median), 75% and 95% percentiles, and maximum, for each peak. This is done for K3 in Fig. 33. The steady state trends observed for the mean are also found when looking at percentiles, with a tremendous contraction of the distribution "bandwidth" for the 3*X* case. It is interesting that for 3*X* there is a transient with impact

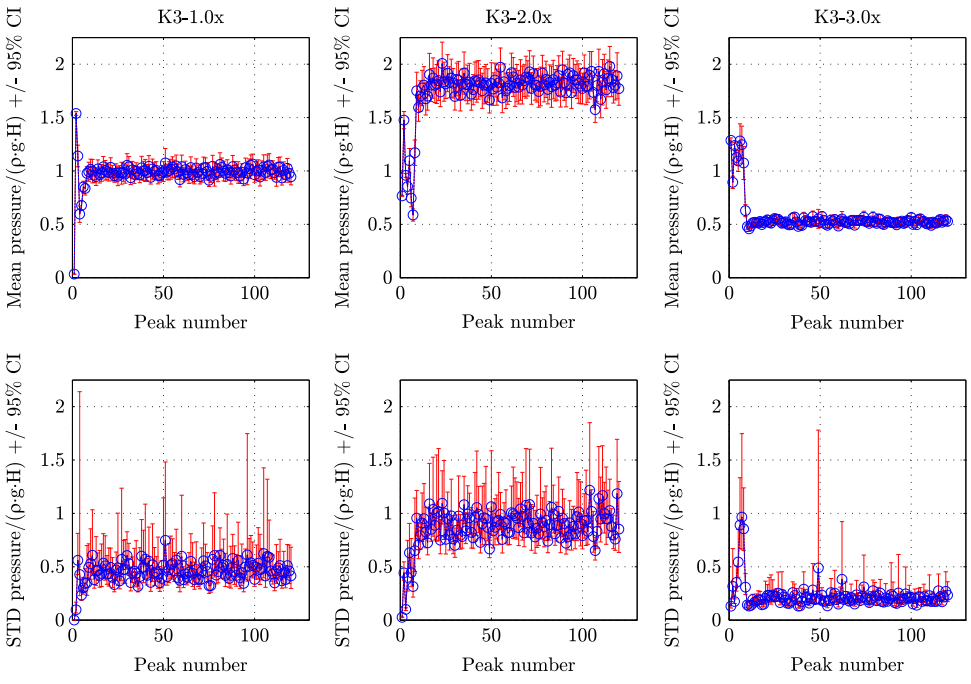

Fig. 32. Roof impacts with oil. Sensor Kulite 3. Various widths. Mean of impacts along successive cycles with confidence interval (top). Standard deviation with confidence interval (bottom).

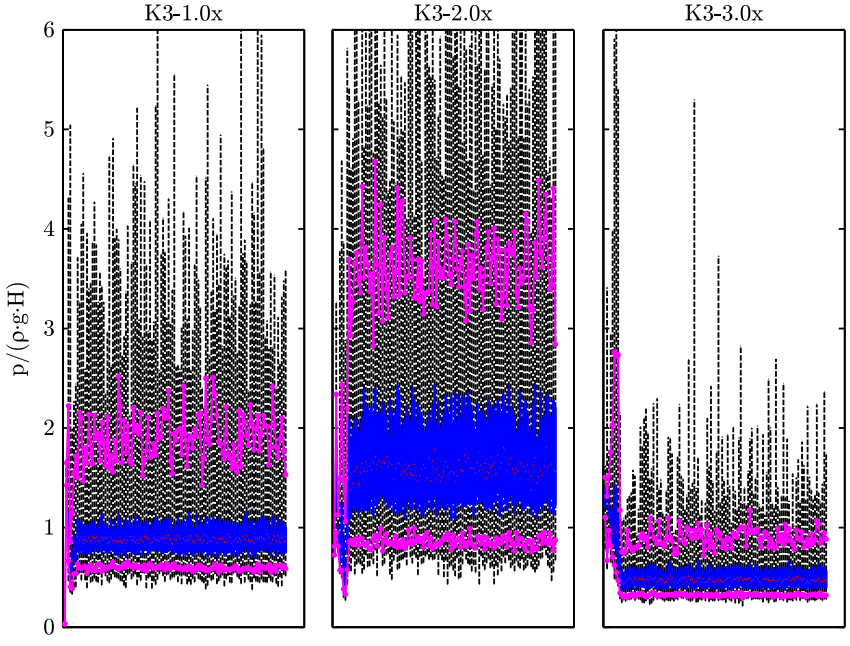

Fig. 33. Roof impacts with oil. Sensor Kulite 3. Various widths. Box plot with minimum, 5%, 25%, 50% (median), 75% and 95% percentiles, and maximum, for each peak. Peak number on the *x*-axis.

values comparable to 2*X*, but the drop after the transient for 3*X* is most interesting. Again, looking at the videos does not seem to shed much light and a deeper investigation, left for future work, is necessary.

Removing the transients from the analysis, empirical exceedance probability graphs are obtained for this same K3 sensor (approximately 12,000 observations). Its associated graphs are presented in Fig. 34. The trends observed in the ensemble domain analysis are confirmed when looking at the low probability levels with some isolated non-representative 3*X* values getting close to the 1*X* case, which definitely requires further research since it radically challenges the trends observed in the rest of the cases.

5. Additional remarks: roof 2*X* water case

5.1. General

In Section 4.1.3 it was shown that, for the 2*X* width tank roof impacts with water, the ensemble statistics displayed a non-stationary behavior. If we look at a series of sample time histories of different experiments for a fixed sensor (Fig. 35), it seems that, at a certain point, a transition from stronger (let us denote them as type A) to weaker (say, type B) impacts usually takes place. These transitional regions are indicated with a double arrow in the figure and their location seems, in principle, random. Complex transient

behaviors can be traced back to the research of Faltinsen et al. (2006), where it was shown that, in certain forcing condition, the free surface elevation induced by sloshing can show transients with variable shape and duration, which can be sensitive to experimental disturbance factors and initial conditions. Faltinsen et al. (2006) do indeed underline this fact by saying that "All of these disturbance factors as well as minor physical factors including breaking phenomena bring to mind the saying of 'gentle touches' to a stone rolling down a mountain can be decisive in determining its future trajectory." (Faltinsen et al., 2006). Although the work of Faltinsen et al. (2006) addressed the free surface and fluid–structure interaction force behavior, herein, the phenomenon under analysis is the pressure resulting from sloshing impacts. It is evident that transient effects associated with the free surface are strictly linked with observations made on impact pressure readings, which is the final quantifiable result of the interaction between the free surface and the tank boundaries.

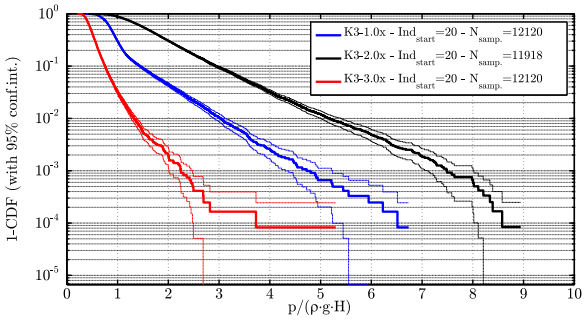

Fig. 34. Roof impacts with oil. Sensor Kulite 3. Various widths. Exceedance probability graph.

Focusing on two of these experiments (Fig. 36), it can be noticed that type A (stronger) impacts and type B (weaker) impacts seem to occur with a different phasing with respect to the motion (which is very repeatable between different experiments). This observation suggests looking at the impact pressure data in combination with the phase lag of the impact with respect to the tank motion. To this end, a joint graph of peaks pressure and phase lag, normalized with the motion period, τ, is presented in Fig. 37 for all experiments. The normalized phase lag τ is zero when the impact occurs at the up-crossing time for the angular motion, and $\tau = 1.0$ at the end of the oscillation period. From the scatter plot in Fig. 37, two clusters can be identified, which allows splitting the impacts in two groups on the basis of the impact phase τ, and which then allows a separate statistical analysis for each single group to be carried out.

5.2. Low probability levels

When extrapolating sloshing impact pressures to low probability levels, no attention is, in general, paid to the type of impact taking place, its relation with the motion, its type, etc. The analysis is usually based on the collection of impact pressure samples, followed by a fitting using, typically, parameterized distributions (Weibull, Generalized Pareto, etc.) (Graczyk et al., 2007; Fillon et al., 2013). The design pressure values are then obtained by extrapolating the model distribution to specified probability levels, typically associated with specified return periods.

As mentioned before, the points in Fig. 37 can be grouped based on the non-dimensional phase lag, τ. Two groups are chosen: $\tau \in [0.23, 0.32]$, which corresponds to type A impacts, and $\tau \in [0.16, 0.22]$, which corresponds to type B impacts. Above $\tau = 0.32$ only the first event peaks, which are not accounted for in the analysis, appear. Between both groups there are a few

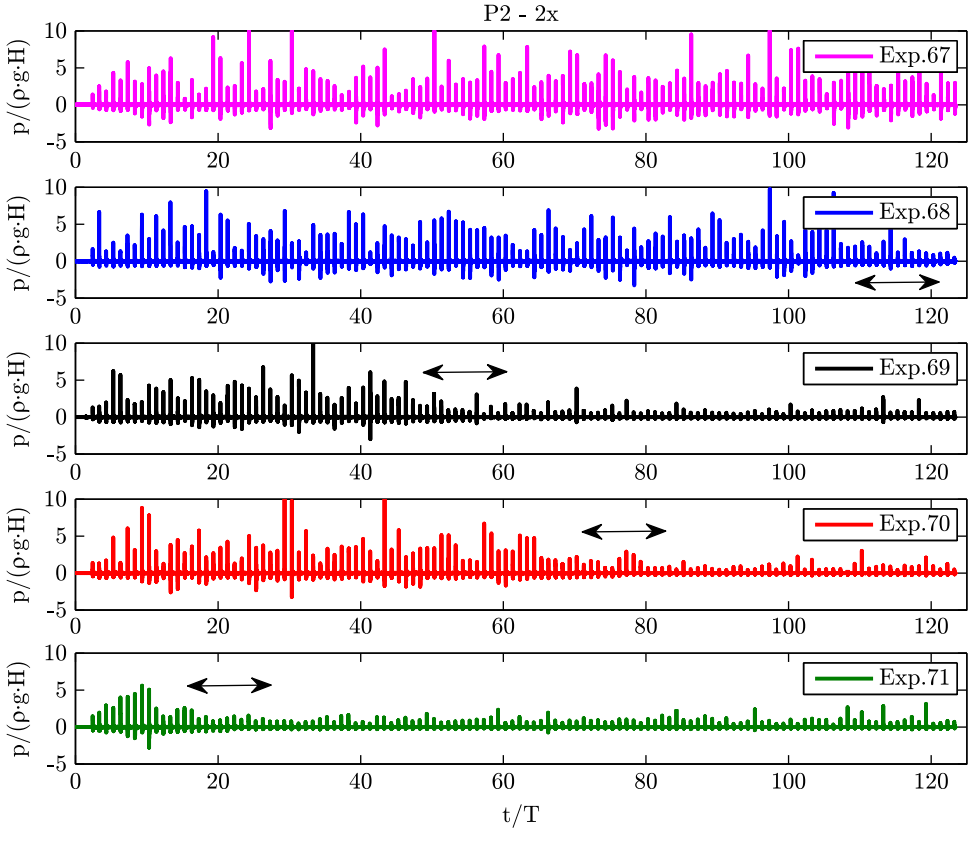

Fig. 35. Roof impacts with water. Sensor PCB 2. 2*X* width. Sample time histories of experiments 67 and following. Double arrows approximately indicate the transition zones between type A (stronger) and type B (weaker) impacts.

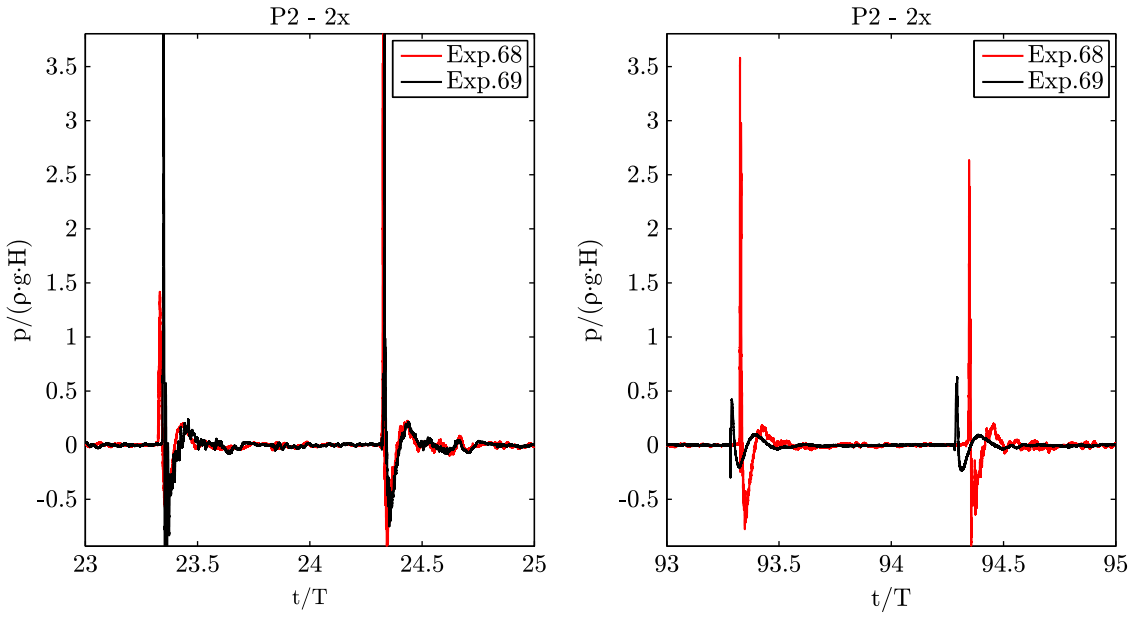

Fig. 36. Roof impacts with water. Sensor PCB 2. 2*X* width. Sample time histories for type A (stronger) and type B (weaker) impacts.

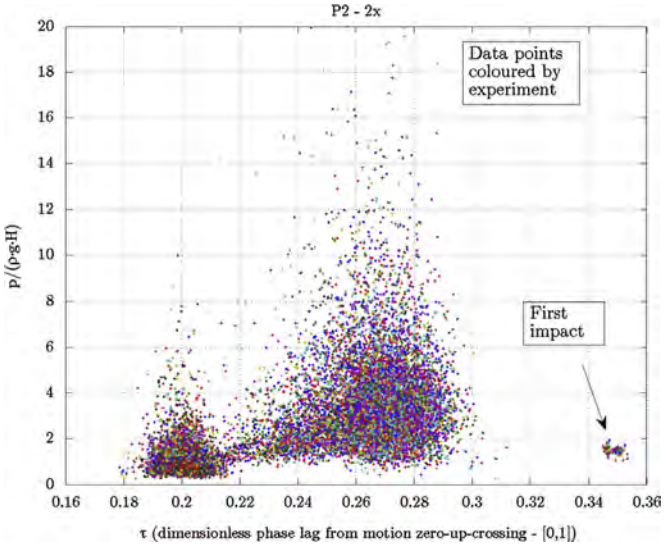

Fig. 37. Roof impacts with water. Sensor PCB 2. 2*X* width. Peaks vs. phase graph.

scattered points which cannot seem to be assigned to any group and are considered to represent transition cases. A histogram of the impact pressure for each group is plotted in Fig. 38. Although already visible from the scatter plot in Fig. 37, it is now even more evident from the histograms in Fig. 38 that impacts with smaller non-dimensional phase lag τ (type B) have an impact pressure distribution shifted towards smaller values, while impact with larger non-dimensional phase lag τ (type A) have an impact pressure distribution which is broader and shifted towards larger impact pressure values.

The exceedance probability graphs of the pressure for both groups are plotted in Fig. 39. As can be appreciated, the low probability levels of these groups are very different and would thus lead to significantly different design pressures. The analysis procedure followed in this section must be considered with caution due to the fact that the analyzed process is non-stationary (see Figs. 25–28). However, this case indicates that when performing a systematic (in a way "blind") statistical analysis collecting together all impact data in a single sample, impacts with inherently different characteristics could be grouped together. Although this is not itself a problem from a statistical point of view, such a grouping could penalize the quality of the distribution model fitting and of the subsequent extrapolation. Instead, identifying the eventual presence of different impact types, and performing separate fittings for each underlying group could possibly allow for better modeling and extrapolation of the data.

6. Conclusions

In the present paper the influence of tank width on impact pressure statistics in regular forced angular motion has been investigated. To this aim:

1. A tank, whose geometry had been used in previous research work, has been designed and built so that its lateral plates can be removed and replaced by ones of varying widths. Four different widths have been considered.
2. The tank has been instrumented with an array of two types of pressure sensors.
3. Two filling levels have been chosen in order to study lateral and roof impacts.
4. The tests have been conducted with both water and oil in order to investigate the influence of the Reynolds number.
5. Tests have been conducted with a rig which allows for one degree of freedom angular motions. The motion has been driven by an electric actuator, whose motion repeatability can be considered extremely good.
6. Motion periods have been chosen in order to have representative free surface shapes.
7. 120 experiments, each comprising 120 peaks, have been conducted allowing for an analysis in time and ensemble domains to be performed.

From the analysis of the obtained data:

1. Lateral impacts with water have displayed a very similar statistical distribution across the range of considered widths. Steady state has been achieved in all cases, with similar mean

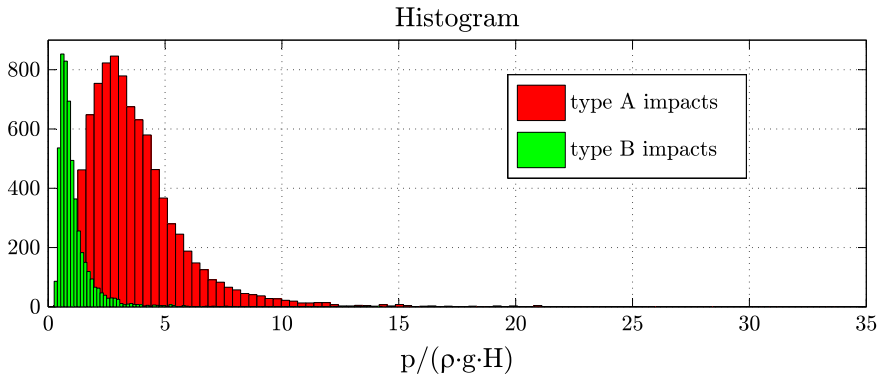

Fig. 38. Roof impacts with water. Sensor PCB 2. 2*X* width. Pressure histogram for different identified impact types.

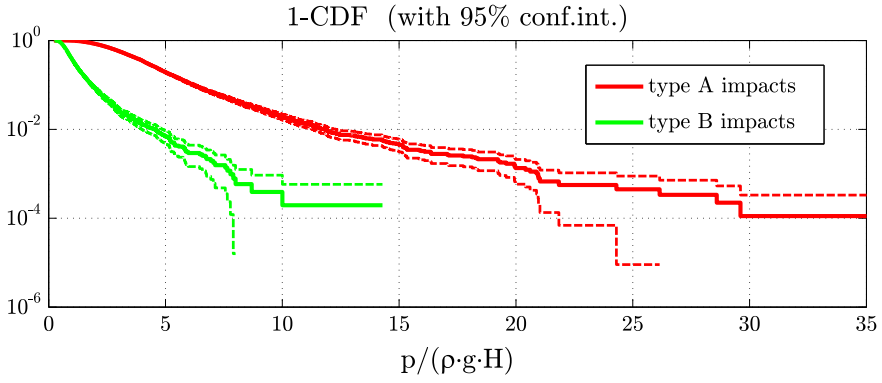

Fig. 39. Roof impacts with water. Sensor PCB 2. 2*X* width. Exceedance probability graph for different identified impact types.

values. Going to low probability levels, the tanks with smaller width have led to larger pressure values, something that can be attributed to the fact that momentum loss due to transversal flow is smaller.

2. Lateral impacts with oil have presented similar mean values across the different considered widths, with a tendency towards an increase of the impact pressure as the width of the tank increases. However, the cases with larger widths have displayed remarkably larger pressure values when going to the low probability levels.
3. Roof impact with water has been the most interesting case. Increasing pressure with width has been found in mean and low probability values. Stationary state has not been achieved for the 2*X* width case within the 120 events considered for each experiment.
4. The 2*X* water roof impact case has been further investigated. Two different impact regimes have been detected based on the phase with respect to the motion. Once a transition takes place, the other regime is not recovered. This explains why no stationary state is achieved in this case. Both states display significantly different statistical properties and low probability pressure values. Considering them all together would make the extrapolation to low probability levels less accurate than being able to identify them and performing a conditional probability analysis. Investigating these multiple type impacts in other cases is left for future work.
5. Roof impact with oil results challenges the trends found in the other configuration, with a dramatic drop of steady state statistics when moving from 2*X* to the largest width tank (3*X*). This case requires further research;
6. Overall, it can be concluded that tank width should be generally considered as a factor to be accounted for when looking at sloshing impact statistics, regardless of eventual negligible influence of this factor in statistical centrality measures, such as mean or median, in certain configurations (e.g. the lateral water cases).

Some future work threads have arisen from the present study, namely

1. Look in detail at sensitivity issues regarding filling level, extending existing literature on single impacts, and tank Plexiglas thickness.
2. Further investigate the influence of the type of impact on the distributions of impact pressure, with particular attention to the tails of such distributions.
3. Extend the present analysis to irregular motions.
4. Perform arrays of longer tests (3 h) for all cases.
5. Look at the roof impact with oil cases in further detail order to understand its results.
6. Assess to what extent the identification of statistics of impacts in regular motion can be useful to understand irregular motion statistics.

A final idea, that we would like to express while closing this paper, is that, even though experiments with regular motions cannot reflect the real stochastic nature of ship motions in ocean environments, they can be used to better understand the physics and to systematically explore the low probability levels of certain types of impacts.

Acknowledgments

The research leading to these results has received funding from the Spanish Ministry for Economy and Competitiveness under

Grant TRA2013-41096-P. Part of this work has been carried out while ASI was at the University of Trieste in 2014, in the framework of a "Lifelong Learning Program – ERASMUS Training Staff" (a.y. 2013/14). The authors thank the GTT staff, namely Laurent Brosset, Eric Gervaise and Thibaut Loysel, for providing access to the PCB sensors set. Finally, the authors are grateful to Hugo Gee for the correction and improvement of the English text and to the two anonymous reviewers for their detailed work and encouraging words.

References

Abrahamsen, B.C., Faltinsen, O.M., 2011. The effect of air leakage and heat exchange on the decay of entrapped air pocket slamming oscillations. Phys. Fluids 23 (10), 102107. http://dx.doi.org/10.1063/1.3638612, URL ⟨http://link.aip.org/link/?PHF/23/102107/1⟩.

Bogaert, H., Lacuteeonard, S., Brosset, L., Kaminksi, M.L., 2010. Sloshing and scaling: results from the Sloshel project. In: International Offshore and Polar Engineering Conference (ISOPE). The International Society of Offshore and Polar Engineers (ISOPE) (June), CA, USA.

Botia-Vera, E., Souto-Iglesias, A., Bulian, G., Lobovský, L., 2010. Three SPH novel benchmark test cases for free surface flows. In: Fifth ERCOFTAC SPHERIC Workshop on SPH Applications.

Bouscasse, B., Antuono, M., Colagrossi, A., Lugni, C., 2013. Numerical and experimental investigation of nonlinear shallow water sloshing. Int. J. Nonlinear Sci. Numer. Simul. 14 (2), 123–138.

Bouscasse, B., Colagrossi, A., Souto-Iglesias, A., Cercos-Pita, J.L., 2014a. Mechanical energy dissipation induced by sloshing and wave breaking in a fully coupled angular motion system. I. Theoretical formulation and numerical investigation. Phys. Fluids (1994–present) 26 (3), 033103. http://dx.doi.org/10.1063/1.4869233.

Bouscasse, B., Colagrossi, A., Souto-Iglesias, A., Cercos-Pita, J.L., 2014b. Mechanical energy dissipation induced by sloshing and wave breaking in a fully coupled angular motion system. II. Experimental investigation. Physics of Fluids (1994–present) 26 (3), 033104. http://dx.doi.org/10.1063/1.4869234.

Brizzolara, S., Savio, L., Viviani, M., Chen, Y., Temarel, P., Couty, N., Diebold, L., Moirod, N., Souto-Iglesias, A., 2011. Comparison of experimental and numerical sloshing loads in partially filled tank. Ships Offshore Struct. 6 (1,2), 15–43.

Bulian, G., Botia-Vera, E., Souto-Iglesias, A., 2014. Experimental sloshing pressure impacts in ensemble domain: transient and stationary statistical characteristics. Phys. Fluids (1994–present) 26 (3), 032102. http://dx.doi.org/10.1063/1.4866315.

Chen, Z., Zong, Z., Li, H.T., Li, J., 2013. An investigation into the pressure on solid walls in 2d sloshing using SPH method. Ocean Eng. 59 (0), 129–141. http://dx.doi.org/10.1016/j.oceaneng.2012.12.013, URL ⟨http://www.sciencedirect.com/science/article/pii/S0029801812004222⟩.

Choi, H.I., Park, J.H., Kwon, S.H., Lee, K.H., Lee, S.B., Yang, Y.J., 2012. An experimental study on hydro-elasticity in sloshing. In: ASME 31st International Conference on Ocean, Offshore and Arctic Engineering, (OMAE2012, June).

Choi, H., Choi, Y., Kim, H., Kwon, S., Park, J., Lee, K., 2010. A study on the characteristics of piezoelectric sensor in sloshing experiments. In: International Offshore and Polar Engineering Conference (ISOPE). The International Society of Offshore and Polar Engineers (ISOPE), CA, USA (June).

Colagrossi, A., Souto-Iglesias, A., Antuono, M., Marrone, S., 2013. Smoothed-particle-hydrodynamics modeling of dissipation mechanisms in gravity waves. Phys. Rev. E 87 (February), 023302.

Delorme, L., Colagrossi, A., Souto-Iglesias, A., Zamora-Rodriguez, R., Botia-Vera, E., 2 2009. A set of canonical problems in sloshing. Part I: pressure field in forced roll. Comparison between experimental results and SPH. Ocean Eng. 36 (2), 168–178. http://dx.doi.org/10.1016/j.oceaneng.2008.09.014.

Diebold, L., 2010. Methodology for LNG terminals. In: International Offshore and Polar Engineering Conference (ISOPE). The International Society of Offshore and Polar Engineers (ISOPE), CA, USA (June).

DNV, 2006. Sloshing Analysis of LNG Membrane Tanks, Classification Notes, No. 30.9. Det Norske Veritas. Technical Report.

Faltinsen, O.M., Rognebakke, O.F., Timokha, A.N., 2006. Transient and steady-state amplitudes of resonant three-dimensional sloshing in a square base tank with a finite fluid depth. Phys. Fluids 18 (1), 012103. http://dx.doi.org/10.1063/1.2160522, URL ⟨http://link.aip.org/link/?PHF/18/012103/1⟩.

Fillon, B., Henry, J., Baudin, E., Diebold, L., Parmentier, G., Derbanne, Q., 2012. Influence of sampling rates on sloshing pressures prediction. In: 22nd International Offshore and Polar Engineering Conference (ISOPE). The International Society of Offshore and Polar Engineers (ISOPE), CA, USA, pp. 409–416 (June).

Fillon, B., Henry, J., Diebold, L., Derbanne, Q., 2013. Extreme values theory applied to sloshing pressure Peaks. In: 23rd International Offshore and Polar Engineering Conference (ISOPE). The International Society of Offshore and Polar Engineers (ISOPE), CA, USA (June).

Fontanarosa, D., Van der Meer, S., Harris, E., Verhaegen, F., 2011. A ct based correction method for speed of sound aberration for ultrasound based image guided radiotherapy. Med. Phys. 38 (5), 2665–2673. http://dx.doi.org/10.1118/1.3583475, URL ⟨http://link.aip.org/link/?MPH/38/2665/1⟩.

Gervaise, E., de Sgraveeze, P.E., Maillard, S., 2009. Reliability-based methodology for sloshing assessment of membrane LNG vessels. In: International Offshore and Polar Engineering Conference (ISOPE). The International Society of Offshore and Polar Engineers (ISOPE), CA, USA (June).

Godderidge, B., Turnock, S., Cowlan, N., Tan, M., 2009. ISOPE 2009 sloshing comparative study: simulation of lateral sloshing with multiphase CFD. In: International Offshore and Polar Engineering Conference (ISOPE). The International Society of Offshore and Polar Engineers (ISOPE), CA, USA (June).

Graczyk, M., Moan, T., 2008. A probabilistic assessment of design sloshing pressure time histories in LNG Tanks. Ocean Eng. 35 (8–9), 834–855. http://dx.doi.org/10.1016/j.oceaneng.2008.01.020, ISSN 0029-8018 URL ⟨http://www.sciencedirect.com/science/article/B6V4F-4RSJF35-2/2/eb37150124347363ad426397dcb63935⟩.

Graczyk, M., Moan, T., Wu, M., 2007. Extreme sloshing and whipping-induced pressures and structural response in membrane LNG tanks. Ships Offshore Struct. 2 (3), 201–216. http://dx.doi.org/10.1080/17445300701423049.

Gran, S., 1981. Statistical distributions of local impact pressures in liquid sloshing. Nor. Marit. Res. 9 (2), 2–12, URL ⟨http://www.scopus.com/inward/record.url?eid=2-s2.0-0019667794&partnerID=40&md5=538f5aab2b5f85bca6ccd2a0c84b52d9⟩.

Hattori, M., Arami, A., Yui, T., 1994. Wave impact pressure on vertical walls under breaking waves of various types. Coast. Eng. 22(1–2), 79–114 (Special Issue Vertical Breakwaters). ISSN 0378-3839. URL ⟨http://www.sciencedirect.com/science/article/pii/0378383994900493⟩http://dx.doi.org/10.1016/0378-3839(94)90049-3.

Khayyer, A., Gotoh, H., 2009. Wave impact pressure calculations by improved SPH methods. Int. J. Offshore Polar Eng. 4 (December (19)), 300–307, ISSN 1053-5381.

Kim, H.I., Kwon, S.H., Park, J.S., Lee, K.H., Jeon, S.S., Jung, J.H., Ryu, M.C., Hwang, Y.S., 2009. An experimental investigation of hydrodynamic impact on 2-D LNG models. In: International Offshore and Polar Engineering Conference (ISOPE). The International Society of Offshore and Polar Engineers (ISOPE), CA, USA (2009).

Kim, S.-Y., Kim, K.-H., Kim, Y., 2012. Comparative study on model-scale sloshing tests. J. Mar. Sci. Technol. 17, 47–58. http://dx.doi.org/10.1007/s00773-011-0144-z, ISSN 0948-4280.

Kim, S.-Y., Kim, K.-H., Kim, Y., 2015. Comparative study on pressure sensors for sloshing experiment. Ocean Eng. 94 (0), 199–212. http://dx.doi.org/10.1016/j.oceaneng.2014.11.014, ISSN 0029-8018 URL ⟨http://www.sciencedirect.com/science/article/pii/S0029801814004260⟩.

Kim, Y., Kim, S.Y., Yoo, W.J., 2010. Statistical evaluation of local pressures in sloshing. In: International Offshore and Polar Engineering Conference (ISOPE), vol. 3. The International Society of Offshore and Polar Engineers (ISOPE), pp. 223–230 (June).

Kim, Y., Kim, S.Y., Kim, J., Lee, J.H., 2013. Comparison of sloshing pressures in 2D and 3D tanks. Int. J. Ocean Syst. Eng. 3 (4), 225–230.

Kimmoun, Ratouis, A., Brosset, L., 2010. Sloshing and scaling: experimental study in a wave canal at two different scales. In: International Offshore and Polar Engineering Conference (ISOPE). The International Society of Offshore and Polar Engineers (ISOPE), CA, USA (June).

Kulite, 2014. Technical Sheet of Pressure Transducer of Type XTEL-190(M).

Kuo, J.F., Campbell, R.B., Ding, Z., Hoie, S.M., Rinehart, A.J., Sandstrom, R.E., Yung, T.W., Greer, M.N., Danaczko, M.A., 2009. LNG tank sloshing assessment methodology for the new generation. In: International Offshore and Polar Engineering Conference (ISOPE). The International Society of Offshore and Polar Engineers (ISOPE), CA, USA (June).

Lafeber, W., Brosset, L., Bogaert, H., 2012. Elementary loading processes (ELP) involved in breaking wave impacts: findings from the Sloshel project. In: 22nd International Offshore and Polar Engineering Conference (ISOPE). The International Society of Offshore and Polar Engineers (ISOPE), CA, USA, pp. 265–276 (2012).

Liu, A.-K., Davis, S.H., 1977. Viscous attenuation of mean drift in water waves. J. Fluid Mech. 81 (01), 63–84. http://dx.doi.org/10.1017/S0022112077001918.

Lobovský, L., Botia-Vera, E., Castellana, F., Mas-Soler, J., Souto-Iglesias A., 2014. Experimental investigation of dynamic pressure loads during dam break. J. Fluids Struct 48, 407–434. ISSN 0889-9746, doi:10.1016/j.jfluidstructs.2014.03.009

Loysel, T., Gervaise, E., Moreau, S., Brosset, L., 2013. Results of the 2012–2013 sloshing model test benchmark. In: 23rd International Offshore and Polar Engineering Conference (ISOPE). The International Society of Offshore and Polar Engineers (ISOPE), CA, USA, June 2013.

Loysel, T., Chollet, S., Gervaise, E., Brosset, L., DeSeze, P.E., 2012. Results of the first sloshing model test benchmark. In: 22nd International Offshore and Polar Engineering Conference (ISOPE). The International Society of Offshore and Polar Engineers (ISOPE), CA, USA (2012).

LRS., 2009. Sloshing Assessment Guidance. Document for Membrane Tank LNG Operations. Lloyds Register of Shipping. Technical Report (May).

Lugni, C., Brocchini, M., Faltinsen, O.M., 2006. Wave impact loads: the role of the flip-through. Phys. Fluids 18 (12), 101–122.

Lugni, C., Brocchini, M., Faltinsen, O.M., 2010a. Evolution of the air cavity during a depressurized wave impact. II. The dynamic field. Phys. Fluids 22 (5), 056102. http://dx.doi.org/10.1063/1.3409491, URL ⟨http://link.aip.org/link/?PHF/22/056102/1⟩.

Lugni, C., Miozzi, M., Brocchini, M., Faltinsen, O.M., 2010b. Evolution of the air cavity during a depressurized wave impact. I. The kinematic flow field. Phys. Fluids 22 (5), 056101. http://dx.doi.org/10.1063/1.3407664, URL ⟨http://link.aip.org/link/?PHF/22/056101/1⟩.

Macià, F., González, L.M., Cercos-Pita, J.L., Souto-Iglesias, A., 2012. A boundary integral SPH formulation. Consistency and applications to ISPH and WCSPH. Prog. Theoret. Phys. 128 (September (3)).
Mehl, B., Oppitz, J., Schreier, S., 2013. Sensitivity study on the influence of the exciting motion in liquid sloshing in a rectangular tank. In: 23rd International Offshore and Polar Engineering Conference (ISOPE). The International Society of Offshore and Polar Engineers (ISOPE), CA, USA (June).
Mehl, B., Schreier, S., Puettmann, A., 2014. Sensitivity study on the influence of the filling height on the liquid sloshing behavior in a rectangular tank. In: 24th International Offshore and Polar Engineering Conference (ISOPE), vol. 3. The International Society of Offshore and Polar Engineers (ISOPE), CA, USA, pp. 278–285 (June).
Morris, J., Monaghan, J., 1997. A switch to reduce sph viscosity. J. Comput. Phys. 136 (1), 41–50.
Neugebauer, J., Moctar, O.E., Potthoff, R., 2014. Experimental and numerical investigation of single impacts in a 2D tank. In: 24th International Offshore and Polar Engineering Conference (ISOPE), vol. 3. The International Society of Offshore and Polar Engineers (ISOPE), CA, USA, pp. 286–295 (June).
Paik, K.-J., Carrica, P.M., 2014. Fluid–structure interaction for an elastic structure interacting with free surface in a rolling tank. Ocean Eng. 84 (0), 201–212. http://dx.doi.org/10.1016/j.oceaneng.2014.04.016, ISSN 0029-8018 URL ⟨http://www.sciencedirect.com/science/article/pii/S0029801814001553⟩.
Park, T.H., Lee, H.H., Shin, H.C., 2011. Regular design wave based sloshing assessment procedure. In: 21st International Offshore and Polar Engineering Conference (ISOPE). The International Society of Offshore and Polar Engineers (ISOPE), CA, USA (June).
Patankar, S., 1980. Numerical Heat Transfer and Fluid Flow, Series in computational methods in mechanics and thermal sciences. Taylor & Francis, London, UK, ISBN 9780891165224 URL ⟨http://books.google.es/books?id=5JMYZMX3OVcC⟩.
Peregrine, D., 2003. Water-wave impact on walls. Annu. Rev. Fluid Mech. 35 (1), 23–43.
Piezotronics, 2008. P.C.B. Model 112A21, ICP Pressure Sensor, Installation and Operating Manual.
Pistani, F., Thiagarajan, K., 2012. Experimental measurements and data analysis of the impact pressures in a sloshing experiment. Ocean Eng. 52 (0), 60–74. http://dx.doi.org/10.1016/j.oceaneng.2012.06.002, ISSN 0029-8018 URL ⟨http://www.sciencedirect.com/science/article/pii/S0029801812001990⟩.
Rafiee, A., Thiagarajan, K.P., Monaghan, J.J., 2009. SPH simulation of 2D sloshing flow in a rectangular tank. In: International Offshore and Polar Engineering Conference (ISOPE). The International Society of Offshore and Polar Engineers (ISOPE), CA, USA (June).
Razzak, S., Amaichan, J., Damion, J.P., Sarraf, C., 2013. Dynamic pressure calibration. In: 23rd International Offshore and Polar Engineering Conference (ISOPE). The International Society of Offshore and Polar Engineers (ISOPE), CA, USA (June).
Repalle, N., Truong, T., Thiagarajan, K., Roddier, D., Seah, R.K.M., Finnigan, T., 2009. The effect of sampling rate on the statistics of impact pressure. In: ASME 29th International Conference on Offshore Mechanics and Arctic Engineering, OMAE2010 (June).
Schreier, S., Mehl, B., 2012. Experimental investigation of 3D sloshing effects in thin rectangular tanks. In: 22nd International Offshore and Polar Engineering Conference (ISOPE). The International Society of Offshore and Polar Engineers (ISOPE), CA, USA (June).
Song, Y., Chang, K.-A., Ryu, Y., Kwon, S., 2013. Experimental study on flow kinematics and impact pressure in liquid sloshing. Exp. Fluids 54 (9), 1592. http://dx.doi.org/10.1007/s00348-013-1592-5, ISSN 0723-4864 URL ⟨http://www.sciencedirect.com/science/article/pii/S0029801812001990⟩.
Souto-Iglesias, A., Botia-Vera, E., Martín, A., Pérez-Arribas, F., 2011. A set of canonical problems in sloshing: experimental setup and data processing. Ocean Eng. 38 (November (16)), 1823–1830.
Topliss, M.E., Cooker, M.J., Peregrine, D.H., 1993. Pressure Oscillations 1078 During Wave Impact on Vertical Walls, vol. 2, Venice, Italy, ASCE, New York, NY, United States, pp. 1639–650. URL ⟨http://www.scopus.com/inward/record.url?eid=2-s2.0-0027264342&partnerID=40&md5=79b9056f0c58386a9633b3562caa0e11⟩.
Yung, T.-W., Sandstrom, R., He, H., Minta, M., 2010. On the physics of vapor/liquid interaction during impact on solids. J. Ship Res. 54 (10), 174–183, URL ⟨http://www.ingentaconnect.com/content/sname/jsr/2010/00000054/00000003/art00003⟩.